Chapter 3
The Electrochemistry of Graphene

When the seagulls follow the trawler, it's because they think sardines will be thrown into the sea. Thank you very much.
King Eric (Cantona)

In this chapter we overview recent developments made by researchers to fundamentally understand the electrochemical behaviour of graphene as an electrode material. However, before considering graphene, it is insightful to first overview graphite and other graphitic surfaces, where a significant amount of information has been gathered over many decades of research, which can be built upon and applied to developing insights into *graphene electrochemistry*.

3.1 Fundamental Electrochemistry of Graphite

Carbon based electrode materials have long been utilised within electrochemistry and have out-performed the traditional noble metals in many significant areas, resulting in them being at the forefront of innovation in this field [1]. This diverse and sustained success is due to carbons structural polymorphism, chemical stability, low cost, wide operable potential windows, relative inert electrochemistry, rich surface chemistry and electro-catalytic activities for a variety of redox reactions [1, 2].

Graphite surfaces are heterogeneous (anisotropic) in nature, with the overall chemical and electrochemical reactivity differing greatly between two distinct structural contributions which are fundamental to the behaviour of graphitic electrodes, namely the edge and basal planes [1]. As mentioned in Chap. 2, the intraplanar (L_a, or *basal plane*) and interplanar (L_c, or *edge plane*) microcrystallic values define distinct structural characteristics of carbon materials (see for example Fig. 3.3), with Highly Ordered Pyrolytic Graphite (HOPG) exhibiting the largest graphite monocrystals; which are found in high quality (ZYA and SPI-1 grade) HOPG. Pyrolytic graphite is a graphitic material with a high degree of preferred crystallographic orientation of the $\boldsymbol{c}$-axes perpendicular to the surface of the substrate (see Fig. 3.1) and is obtained by graphitisation heat treatment of pyrolytic carbon or by Chemical Vapour Deposition (CVD) at extremely high temperatures ($\sim$2,500 °K). The hot working of pyrolytic graphite by annealing under compressive stress at high temperatures produces HOPG. The crystal structure of HOPG is shown in Fig. 3.1 which is characterised by an arrangement

D. A. C. Brownson and C. E. Banks, *The Handbook of Graphene Electrochemistry*,
DOI: 10.1007/978-1-4471-6428-9_3, © Springer-Verlag London Ltd. 2014

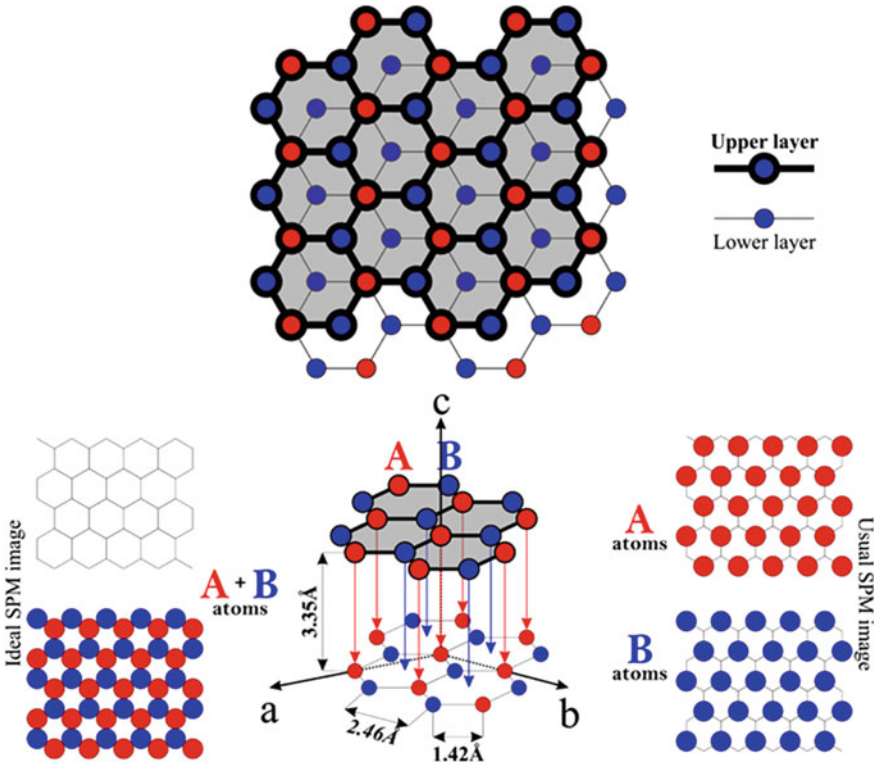

Fig. 3.1 A schematic representation of the structure of a bulk *hexagonal* graphite crystal showing the bulk unit cell. *Side insets*: *Top* view of the basal plane of graphite and a schematic representation of the surface structure (carbon atoms) of graphite, where every other atom is enhanced (*right-side inset*) and viewed under ideal conditions, and where every single atom is seen (*left-side inset*). Figure reproduced from Ref. [3]

of carbon atoms in stacked parallel layers, where the graphite structure is described by the alternate succession of these identical staked planes. Carbon atoms within a single plane of graphite have a stronger interaction than with those from adjacent planes (which explains the cleaving behaviour of graphite). Note that a single-atom thick form of carbon is known as graphene, where the lattice consists of two equivalent interpenetrating triangular carbon sub-lattices denoted A and B (see Fig. 3.1) where each one contains a half of the carbon atoms. Each atom within a single plane has three nearest neighbours: the sites of one sub-lattice (A—marked by the red layer in Fig. 3.1) are at the centres of triangles defined by three nearest neighbours of the other one (B—marked by the blue layer in Fig. 3.1). The lattice of graphene has two carbon atoms, designated A and B, per unit cell, and is invariant under 120° rotation around any lattice site.

The term "mosaic spread" is used to characterise the quality of HOPG which is performed via X-ray crystallography with CuKα radiation by measuring

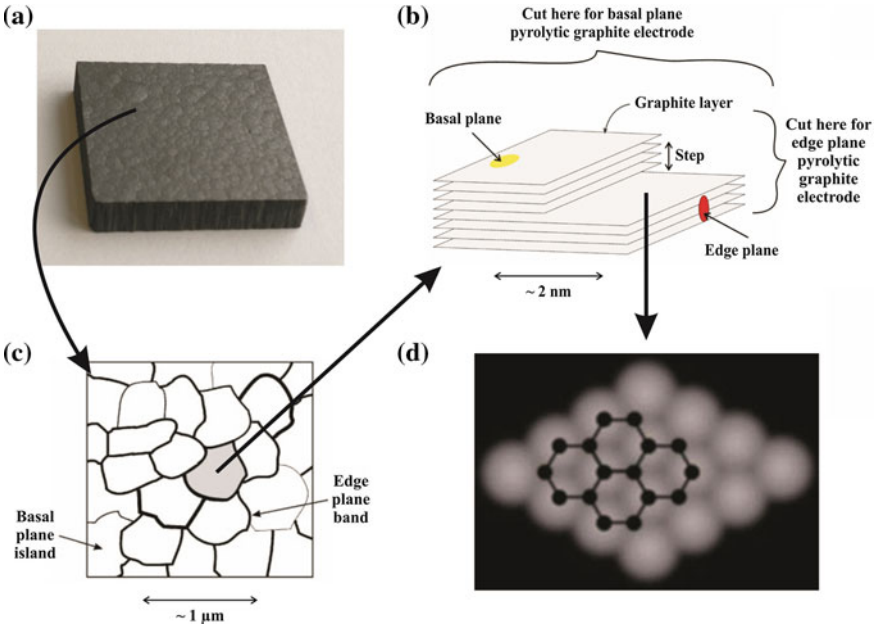

Fig. 3.2 **a** Image of a commercially available slab of HOPG. **b** Schematic representation of the side on view of a HOPG surface, highlighting its basal plane and edge plane like- sites/defects which exhibit contrasting behaviours in terms of electrochemical activity, where electron transfer kinetics of the latter are overwhelmingly dominant over that of the former which in comparison are relatively (electrochemically) inert. **c** A schematic representation of a HOPG surface showing the discrete basal plane and edge plane islands. **d** A typical STM image of a HOPG surface with the corresponding fragment of the graphene structure superimposed

(in degrees) a Full Width at Half Maximum (FWHM) of the rocking curve. Disorder in the HOPG produces broadening of the (002) diffraction peak where the more disorder, the wider the peak becomes. The measured value of the mosaic spread depends not only on crystal quality, but also on the energy and the cross section of the reflected beam. Figure 3.2a depicts a picture of a commercially obtainable HOPG 'slab' which in this case is 'Grade SPI-1', which has the tightest mosaic spread of 0.4° (±0.1°) demonstrating outstanding crystalline perfection. Note that the ZYB, ZYD and ZYH grade HOPG results in mosaic spread values of 0.8° (±0.2°), 1.5° (±0.3°) and 3.5° (±0.5°) respectively.

Shown in Fig. 3.2 is a top-down schematic representation of the HOPG surface, which depicts the discrete edge plane and basal plane islands, and a side on view highlighting the edge plane and basal plane like- sites/defects which are defined by the quality of the chosen HOPG. Also shown in Fig. 3.2d is a Scanning Tunnelling Microscopy (STM) image of a HOPG surface, highlighting the hexagonal crystal structure. Note that in terms of the electrochemical performance of graphitic materials, it has been deduced (see Sect. 3.1.2) that the electrochemical activity of edge and basal planes is distinct such that electrochemical reactions on the edge

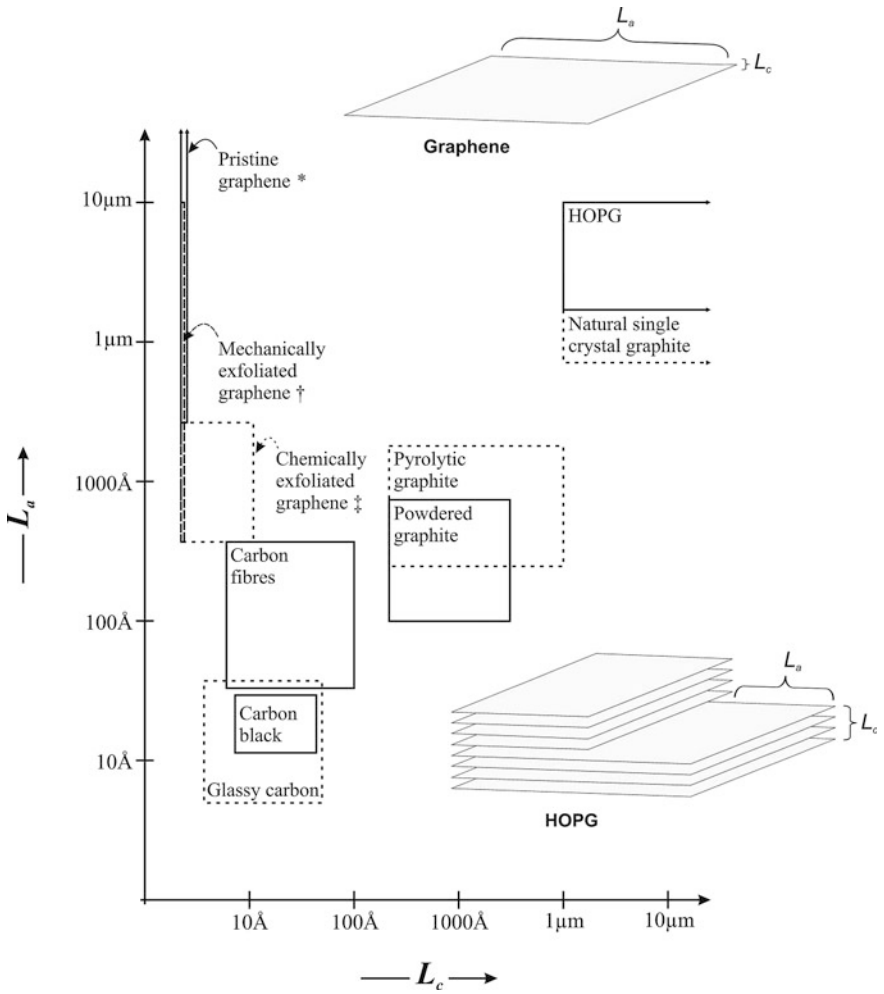

Fig. 3.3 The approximate ranges of L_a and L_c values for various sp^2 carbon materials. Note, there is large variation of L_a and L_c with sample history and thus the values shown should be considered representative, yet approximate. *: Pristine graphene; commercially available from 'Graphene Supermarket', produced via a substrate-free gas-phase synthesis method. [7, 8] ‡: Chemically exfoliated graphene; commercially available from 'NanoIntegris', produced via a surfactant intercalation process—note that this range is also representative of graphene produced through other chemical exfoliation routes such as the reduction of GO. [9, 10] †: Mechanically exfoliated graphene was fabricated through the so-called 'scotch tape method'. Note that graphene synthesised via CVD has been excluded given that crystal size and quality are large variables through this route, however single graphene crystals with dimensions of up to 0.5 mm have been reported. [11, 12] A schematic representation of the L_a and L_c microcrystalline characteristics of graphene and *HOPG* is also shown. Reproduced from Ref. [13] with permission from The Royal Society of Chemistry

plane like- sites/defects are anomalously faster (exhibit greater reactivity) over that of the basal planes [4–6]. In terms of relating this to other carbon allotropes, Fig. 3.3 shows the range of L_a and L_c values for a collection of other graphitic forms where it is evident that HOPG has L_a and L_c values exceeding 1 μm while polycrystalline graphite has values from 10 to 100 nm and carbon from 1 to 10 nm. Graphene, which is readily obtainable from a range of commercial suppliers is also included, highlighting the variation in structure that can be obtained, which is of course dependant on the fabrication methodology; with L_a values for graphene ranging from below 50 up to 3,000 nm and larger, and of course true (monolayer) graphene possesses an L_c value of 0.34 nm.

3.1.1 The Electronic Properties (DOS) of Graphitic Materials

An important parameter of an electrode material is its electronic properties, namely, the Density Of electronic States (DOS) which varies greatly on the different forms of graphite. Gold typically has a DOS of 0.28 states $atom^{-1}$ eV^{-1} with the high conductivity of gold arising from the combination of a high proportion of atomic orbitals to form bands with a high density of electronic states [1]. For a given electrode material, a higher DOS increases the possibility that an electron of the correct energy is available for the electrode to transfer to an electroactive species; the heterogeneous electron transfer rate is thus dependent on the DOS of the electrode material [1]. HOPG has a DOS which overall is lower than that of metal, but is particularly low near the Fermi level and has been reported to have a minimum DOS of around 0.0022 states $atom^{-1}$ eV^{-1}, which is about 0.8 % that of gold [1].

The DOS at graphitic materials can be increased through disorder such that electroactive species exhibit increasing electron transfer rates but by varying amounts. In terms of outer-sphere electron transfer systems, disorder increases the rate by modifying the electronic structure of the carbon while for inner-sphere systems, specific surface interactions also contribute (see later, Box 3.1) [14]. A perfect/pristine basal surface of HOPG has no edge plane (in theory), no location for surface functional groups and there are no dangling bonds since the carbon atoms have satisfied valances [1]. When disorder is introduced, such as through mechanical roughening of the electrode surface, the surface is disturbed such that surface defects are introduced, viz edge plane sites, which increase the DOS [1]. A further extreme is the complete change of a graphitic surface to a different structural composition (L_a and L_c; see Figs. 3.2 and 3.3) towards that of Edge Plane Pyrolytic Graphite (EPPG) which has a high proportion of edge plane sites and thus improvements in electron transfer are observed [1, 13].

Electronic properties of graphitic materials are thus highly relevant and critical, where the energy-dependant densities of electronic states have major effects on

electron transfer. Note that graphitic materials differ greatly in their surface chemistry, which is also critical when understanding electrochemical processes at these materials [1]. Such insights from graphitic materials can be applied for the case of graphene. In terms of the DOS for graphene, insights from HOPG (multiple layers of graphene) can be illuminating to understand its electrochemical reactivity. For a diffusional outer-sphere electron transfer process, the standard electrochemical rate constant, k^0, can be defined as [15, 16]:

$$k^o = \frac{(2\pi)^2 \rho \left(H_{DA}^0\right)^2}{\beta h (4\pi \Lambda)^{1/2}} \exp\left[-\frac{\Lambda}{4}\right] I(\theta, \Lambda) \tag{3.1}$$

where ρ is the density of electronic states in the electrode material, H_{DA}^o is the electronic coupling matrix at the closest distance of approach, $\Lambda = (F/RT)\lambda$, where λ is the reorganisation energy, β is its associated electronic coupling attenuation coefficient, h is Planck's constant, F is the Faraday constant, R the gas constant and T the absolute temperature. $I(\theta, \Lambda)$ is an integral give by [16]:

$$I(\theta, \Lambda) = \int_{-\infty}^{\infty} \frac{\exp\left[-(\varepsilon - \theta)^2/4\Lambda\right]}{2\cosh[\varepsilon/2]} \mathrm{d}E \tag{3.2}$$

where $\theta = F/RT(E - E_f^0)$, and E_f^0 is the formal potential. Thus from inspection of Eq. (3.1) there is a direct relationship between the DOS and the standard electrochemical rate constant (k^o). Thus this can be interpreted for graphite as the DOS varies significantly as a function of energy with a minimum at the Fermi level [16]. For example, it has been shown that electron transfer is non-adiabatic and that the rate of electron transfer varies as a function of the applied potential, as is evident from inspection of Eq. (3.1) for outer-sphere redox systems [16].

It has been reported that the basal plane of pristine graphene has a DOS of 0 at the Fermi level, which was shown to increase with edge plane defects [17–19]. Conversely the edge plane sites on graphene nanoribbon's zigzag edge have been reported to possess a high DOS [19]. Other work has shown that depending on how the edge of graphene terminates, [20] a variable DOS is observed [21]. Thus, graphene, a single layer comprising HOPG, should in theory act similar in terms of its DOS to that observed for HOPG (see above); that is, pristine graphene with no defects should exhibit poor electrochemical behaviour and on the contrary graphene possessing a high degree of defects should exhibit improvements in the observed electrochemical rate constant.

There is a wealth of literature on graphene which reports that the edge of graphene is particularly more reactive than its side (basal plane). For example, using Raman spectroscopy Strano and co-workers [22] report the reactivity of graphene, that being single-, double-, few- and multi-layer towards electron transfer chemistries with 4-nitrobenzenediazonium tetrafluoroborate. Strano et al. [22]

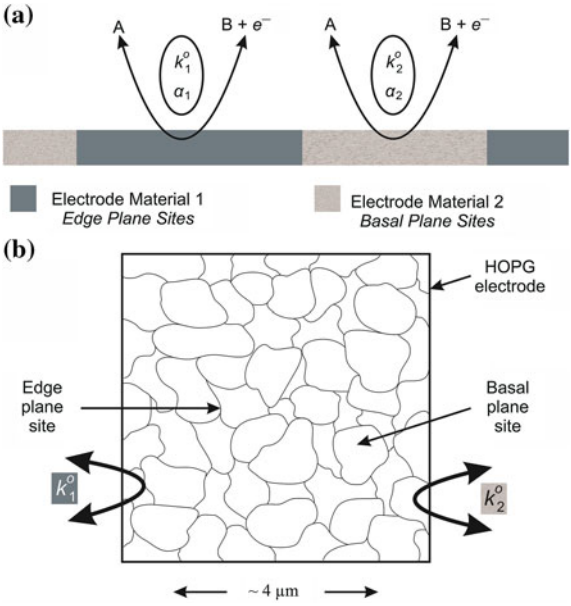

Fig. 3.4 **a** Schematic representation of an electrochemical reaction occurring on the same electrode surface with different Butler-Volmer characteristics; and a *top*-down perspective (**b**)

interpret their observations with consideration to the Gerischer−Marcus theory which states that the charge transfer depends on the electronic DOS of the reacting species and is not restricted to their Fermi levels only. The observed electron-transfer reaction rate ($k^{OBS}_{Graphene}$) is given by Eq. (3.3) where $W_{OX}(\lambda, E)$ is the distribution of the unoccupied redox states of the electron acceptor in solution given by Eq. (3.4). The $DOS_{Graphene(N=1/N=2)}$ is the electronic density of states of graphene for $N = 1$, and of double layer graphene for $N = 2$ and ε_{OX} is the proportionality function [22].

$$k^{OBS}_{Graphene} = \upsilon_n = \int_{E_{redox}}^{E_F^{Graphene}} \varepsilon_{OX}(E) DOS_{Graphene(N=1/N=2)}(E) W_{OX}(\lambda, E) dE \tag{3.3}$$

$$W_{OX}(\lambda, E) = \frac{1}{\sqrt{4\pi\lambda kT}} exp\left(-\frac{(\lambda - (E - E_{redox}))^2}{4\lambda kT}\right) \tag{3.4}$$

Calculations presented by Strano et al. suggest that double layer graphene is almost 1.6 times more reactive than single layer graphene [22]. Thus based on the DOS, it is clear that double layer graphene (or further graphitic structures consisting of multiple graphene layers) is more reactive than single layer graphene, which has clear implications for graphene as an electrode material; it is this we explore in more detail in Sect. 3.2.

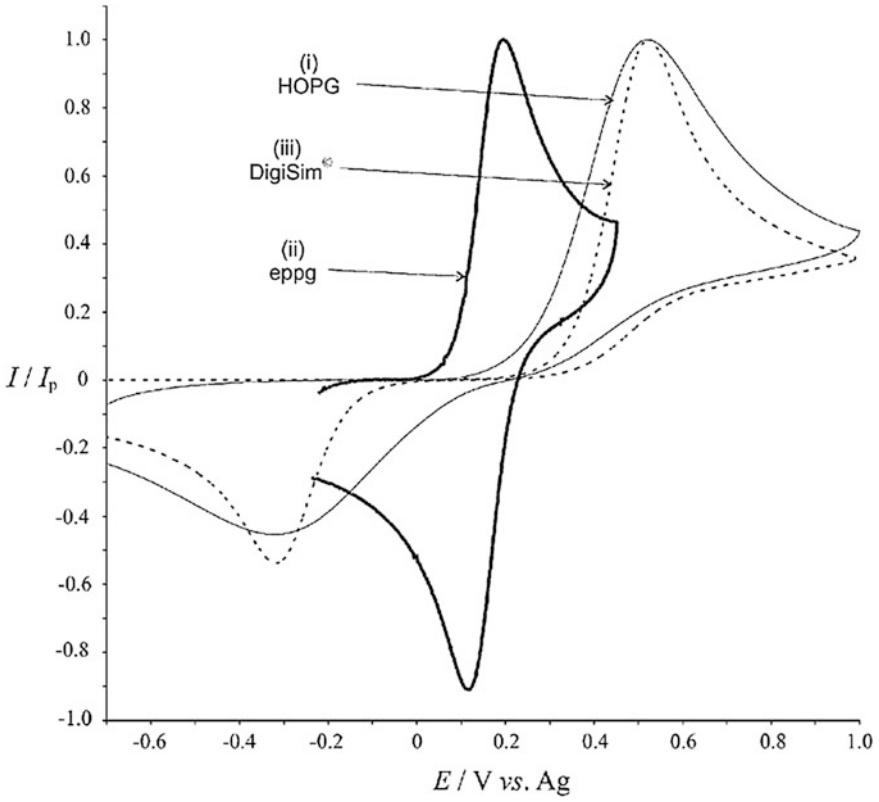

Fig. 3.5 Cyclic voltammograms recorded at 1 Vs^{-1} for the oxidation of 1 mM ferrocyanide in 1 M KCl at a basal plane *HOPG* electrode and an *EPPG* electrode. The *dashed line* voltammogram is the simulated fit using linear diffusion only (DigiSim$^{(R)}$). Reproduced from Ref. [23] with permission from The Royal Society of Chemistry

3.1.2 Electrochemistry of Heterogeneous Graphitic Surfaces

The electrochemical characteristics and reactivity of HOPG has been fully understood by Compton and co-workers, [5] who have shown convincing evidence that edge plane sites/defects are the predominant origin of electrochemical activity. Figure 3.4a shows a schematic representation of the heterogeneous HOPG surface (see Fig. 3.2b and c) which has the two distinctive structural contributions, namely edge plane and basal plane sites, each with their own electrochemical activity and thus differing Butler-Volmer terms, k^o and α.

Using a simple redox couple, Fig. 3.5 depicts the voltammetry obtained when using either a Basal Plane Pyrolytic Graphite (BPPG) (i) or (ii) an EPPG electrode of HOPG, and the responses are compared with numerical simulations (iii) assuming linear diffusion only, in that, all parts of the electrode surface are uniformly (incorrectly) electrochemically active. Two features of Fig. 3.5 are to be

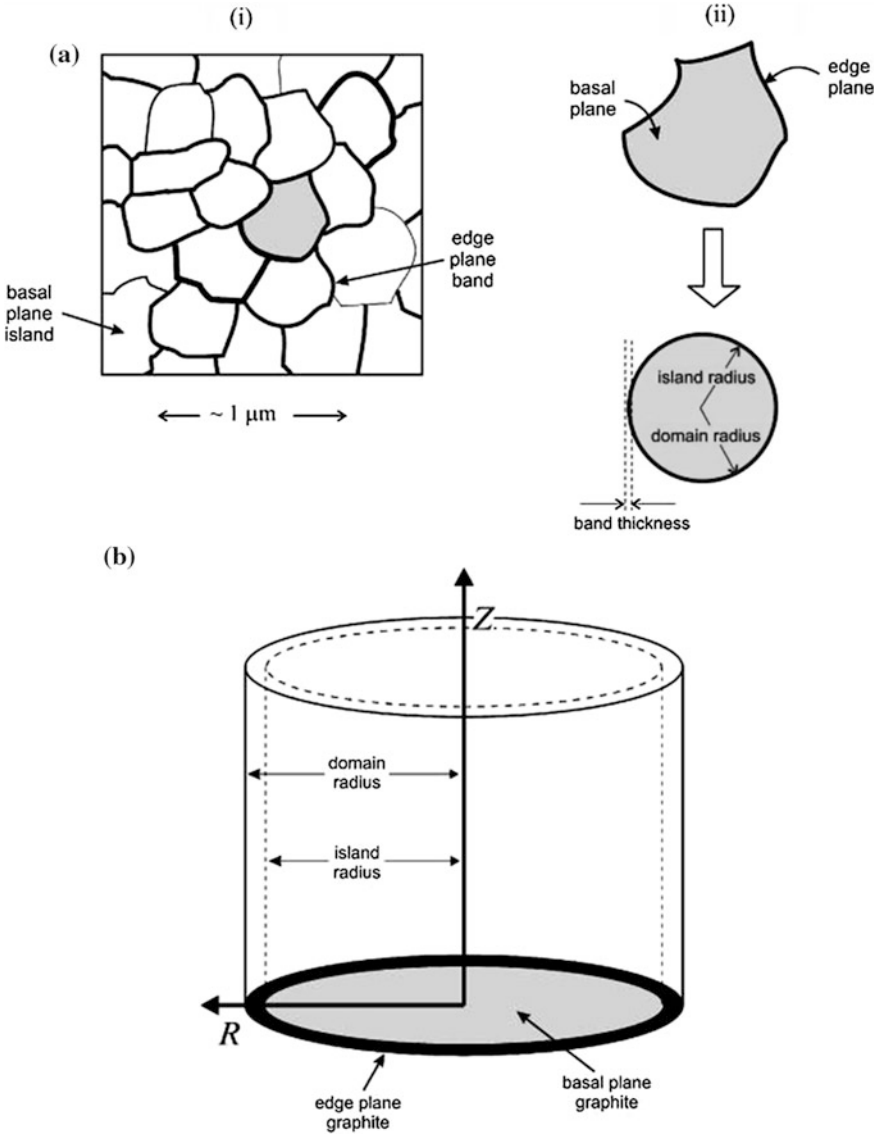

Fig. 3.6 Schematic diagrams showing: **a** (*i*) the overhead view of a section of the basal plane HOPG surface and (*ii*) the approximation of each island/band combination as a partially covered *circular disc* of the same area; **b** the resulting diffusion domain from the approximation in (**a**) (*ii*) and the cylindrical coordinate system employed. Reproduced from Ref. [23] with permission from The Royal Society of Chemistry. Note that the island radius is termed R_b and the domain radius is R_0

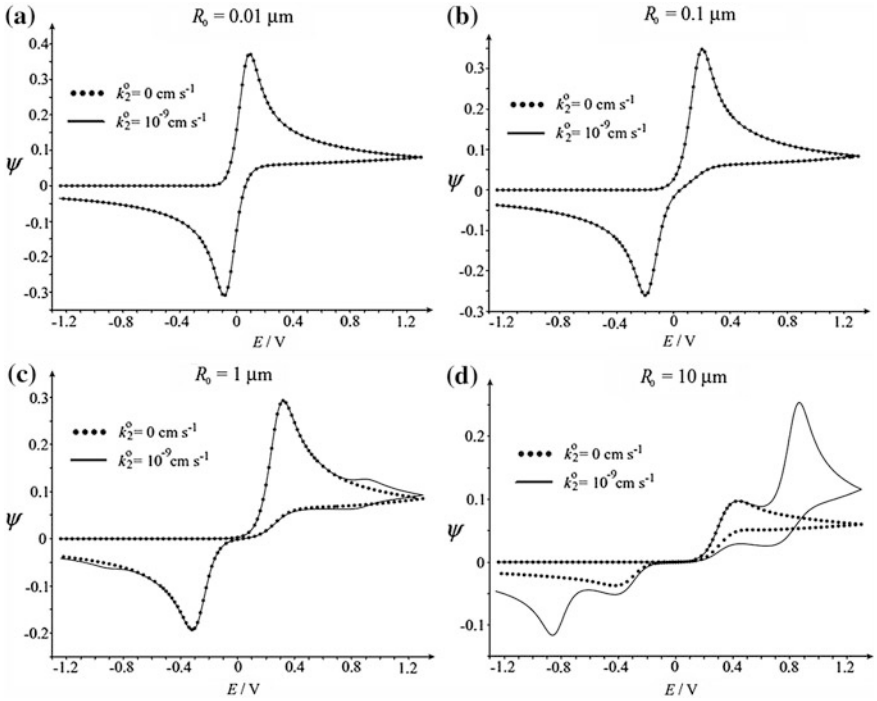

Fig. 3.7 *Solid curves* are simulated dimensionless current cyclic voltammograms for diffusion domains where $D = 6.1 \times 10^{-6}$ cm^2 s^{-1}, $k_1^o = k_{edge}^o = 0.022$ cm s^{-1}, $k_2^o = k_{basal}^o = 10^{-9}$ cm s^{-1}, $\upsilon = 1$ V s^{-1}, the band thickness is 1.005 nm and the domain radius is **a** 0.01 μm **b** 0.1 μm **c** 1 μm and **d** 10 μm. Overlaid in each section are the simulated inert equivalents (*dotted curves*), i.e., $k_2^o = k_{basal}^o = 0$ cm s^{-1}. Reprinted from Ref. [5] with permission from Elsevier

noted: (1) there is a significant increase in the peak-to-peak separation, ΔE_P, observed for (iii) over the EPPG voltammetric response (ii); (2) the fit to the 'linear diffusion' only (iii) simulation is not fully satisfactory, especially in the return scan where a significantly lower back peak (current) is observed than expected [23]. It has been shown that the observed voltammetric signature (i) can be correctly and quantitatively simulated through considering the HOPG surface (as shown in Figs. 3.2 and 3.4) to be a heterogeneous surface consisting of edge plane nano bands which have been concluded to be exclusively the sites of electro-catalysis whereas the basal plane 'islands' are electro-catalytically inert [5].

Figure 3.6 depicts how the HOPG surface has been simulated using numerical simulation via the diffusion domain approach, where each basal plane island and the surrounding edge-plane band is considered as a circular disc of edge-plane graphite partially (or almost completely) covered with basal plane graphite, such that the areas of edge and basal plane are consistent. Since the island and band are surrounded by other island/band combinations, little or zero net flux of electro-active species will pass from one island to its neighbour [5, 23].

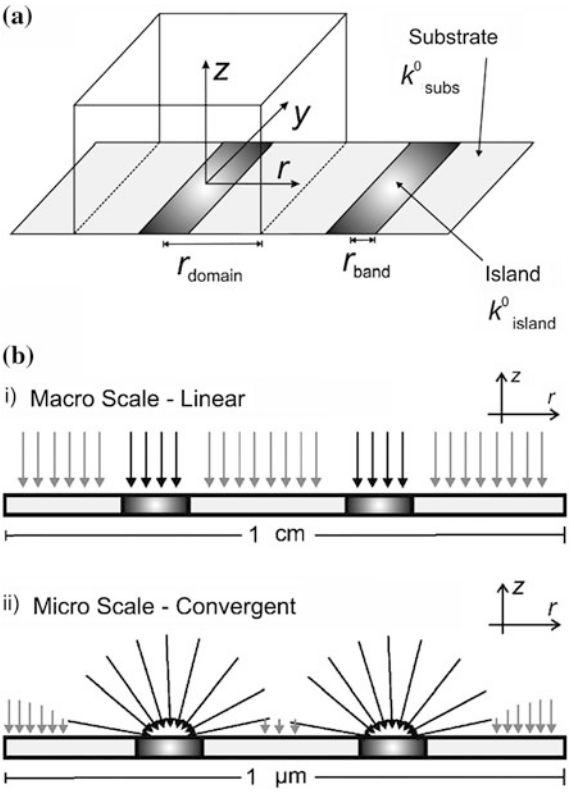

Fig. 3.8 **a** The surface is split into a series of identical domains (unit cells), namely band islands. **b** Schematic showing the difference between diffusion to macro- (*i*) and micro- (*ii*) scale electrode systems. The *darker* area represents the island (r_{band}) with the faster kinetics. Reproduced from Ref. [24] with permission from The Royal Society of Chemistry

The circular discs are treated as independent entities with cylindrical walls through which no net flux can pass. These unit cells are better known as diffusion domains and are illustrated in Fig. 3.6 where the two electrode materials (edge plane and basal plane) are highlighted. The voltammetric response of the whole HOPG electrode is therefore the sum of that for every domain on the electrode surface. Also shown is a single diffusion domain unit cell and the cylindrical polar coordinate system employed where interacting cylindrical units of radius R_0 are centred around a circular block of radius R_b, where the fractional coverage of the domain, $\theta = R_b^2/R_0^2$ such that the surface areas of the basal sites and edge sites are given by $(1-\theta)\pi R_0^2$ and $\theta\pi R_0^2$ respectively, allowing the effect of varying the edge sites while keeping the surface coverage constant. The island radius is termed as R_b and R_0 is the domain radius which includes the width of the edge plane site/band. As is evident from Fig. 3.7, the ΔE_P of the edge plane nano band signal depends strongly on the edge plane coverage, and the domain size has little or no influence on the observed voltammetry of the three smaller domains due to the depleting effect of non-linear diffusion which becomes less relevant as the domain sizes increase. Note that the maximum lateral grain size of HOPG is 1–10 μm resulting in a maximum R_0 of $\sim$0.5–5 μm, the edge plane coverage is such that the basal plane

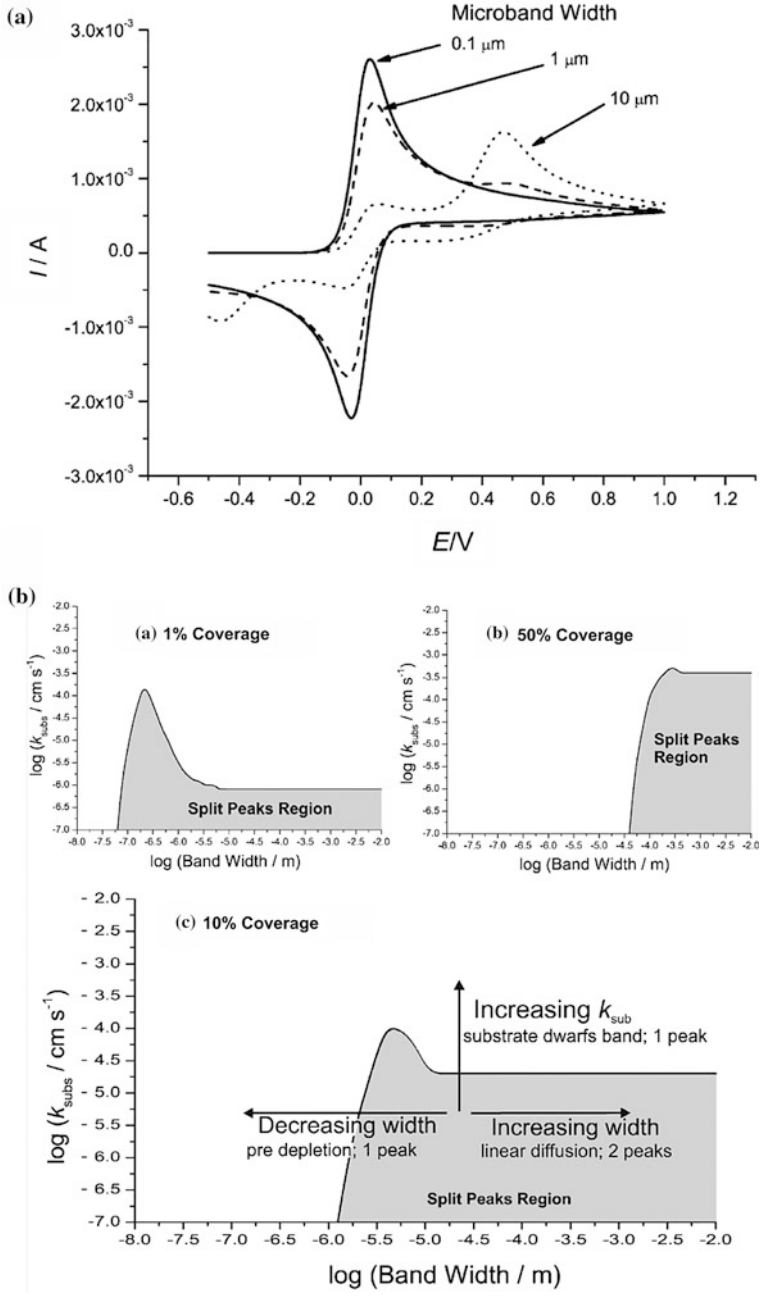
(a)
Microband Width
0.1 μm
1 μm
10 μm
I / A
E/V
(b)
(a) 1% Coverage
Split Peaks Region
(b) 50% Coverage
Split Peaks Region
(c) 10% Coverage
Increasing k_{sub}
substrate dwarfs band; 1 peak
Decreasing width
pre depletion; 1 peak
Increasing width
linear diffusion; 2 peaks
Split Peaks Region
log (k_{subs} / cm s^{-1})
log (Band Width / m)

◀ **Fig. 3.9** **a** Voltammetry of a one-electron transfer process at an electrochemically heterogeneous electrode consisting of an array of microbands ($k^o = 10$ cm s^{-1}) distributed over a substrate material ($k^o = 10^{-6}$ cm s^{-1}) of area 1 mm^2 and a surface coverage of the bands of 10 % at a scan rate of 0.1 Vs^{-1}. The diffusion coefficient of all species is 10^{-5} cm^2 s^{-1} with an initial concentration of 10 mM. The voltammetry transitions from 1 peak to 2 peaks as the width of the band (labelled) is increased. **b** Schematics showing the region of the 'Band Width'-'Substrate rate constant' space for which there are two peaks in the forward sweep of a cyclic voltammogram at band surface coverages of (*a*) 1 % (*b*) 50 % and (*c*) 10 %. Scan rate = 0.1 Vs^{-1}; diffusion coefficient = 10^{-5} cm^2 s^{-1}; island rate constant $k^o_{band} = 10$ cm s^{-1}. Reproduced from Ref. [24] with permission from The Royal Society of Chemistry

is effectively inert [23] and the HOPG response can be assigned to nano bands of edge plane graphite with the basal plane islands having no contribution.

Further work from the Compton group has explored the 'double peak concept', [24] modelling a HOPG surface as an array of microbands; the unit cell is shown in Fig. 3.8a while Fig. 3.9 depicts the response of an electrochemically heterogeneous surface highlighting the effect of microband width along with the domain coordinates utilised where the fractional coverage of the surface covered is given by: $\theta_{band} = r_{band}/r_{domain}$. Figure 3.9a shows that as the width of the band is increased the diffusion profile changes from being largely convergent, as shown schematically in Fig. 3.8b, to that of linear which is seen as one peak becoming two and a decrease in the peak current is also evident; note that Chap. 2 considered the case of mass transport. The depletion of the electroactive species above the electrochemically slower substrate proceeds to a greater extent so the substrate has less of an influence on the diffusion of the electroactive species and thus less of an influence on the observed voltammetry [24]. The depletion, known as the diffusion layer, is given by Eq. (2.32) where for voltammetry t is replaced by: '$\Delta E/\upsilon$' where ΔE is the potential range over which electrolysis occurs and t (referred to as t_{peak}: below) is the time taken to sweep the potential from its initial value to the point where the current reaches a maxima. It has been shown that [24]:

$$\sqrt{2Dt_{peak}} \gg r_{sep} \tag{3.5}$$

where

$$r_{sep} = \frac{1}{2}(r_{domain} - r_{band})$$

where r_{band} is the width of the edge plane site and r_{domain} accounts for the edge plane site *plus* the basal plane site (see Fig. 3.8a). In this case, the inter-band separation is small compared to the extent of diffusion parallel to the electrode surface and only one peak will be observed in the voltammetry. Figure 3.9b shows the effect of the band width upon k^o_{subs} and in which region split peaks will be observed. In the case that there is a large domain width, $\sqrt{2Dt_{peak}} \ll r_{sep}$, such that the voltammetry will be a superposition of the voltammetry of the band and substrate in isolation where diffusion to each will be linear in nature.

If the heterogeneous rate constants on the two electrode surfaces are similar, two peaks will be observed arising at similar potentials which will merge into one larger peak. If $k^o_{band} \gg k^o_{subs}$ (i.e. $k^o_{edge} \gg k^o_{basal}$) two peaks will be observed if the k^o_{subs} has measurable activity; however it has been shown that this is not the case and only the k^o_{band} is active, or sometimes reported as anomalously faster over that of k^o_{subs} [4].

The rate of electron transfer for basal plane sites has been reported to correspond to $\sim 10^{-9}$ cm s^{-1} for the oxidation of ferrocyanide and is considered to be possibly even zero [4–6]. *How does one know that this is actually correct?* As shown in Fig. 3.9a, a strangely distorted voltammogram would be observed in the limit of very low defect density [23]. Due to the fact that two peaks have never been observed experimentally, it is generally accepted that edge plane electron transfer kinetics are anomalously faster over that of basal plane; the latter is sometimes referred to as being inert [5, 6, 23]. Interested readers are directed to the elegant work of Davies et al. and Ward et al. to further appreciate this work [5, 24].

Further evidence on the role of edge plane sites *versus* basal plane sites has been reported [4] by the selective blocking of the basal plane sites of HOPG with a polymer whilst the edge plane sites were left exposed. Identical voltammetric behaviour was observed with this modified surface when compared to that of the initial bare electrode and with numerical simulations, confirming the edge planes to be the sites of electrochemical activity; Fig. 3.10 depicts how this was achieved.

During each stage (as shown in Fig. 3.10) each surface was voltammetrically examined and the corresponding voltammograms are depicted in Fig. 3.11. As shown in Fig. 3.11 it is evident that the final stage is nearly identical with that of stage 1 (a freshly produced HOPG surface) despite the basal plane sites being covered. The small deviation is reported to be due to the treatments that the electrode has undergone and a slight loss in activity of the edge plan sites. In the case of the modified electrode, Fig. 3.11d, only the edge-plane steps located along the bottom of the nanotrenches are exposed to the solution such that an array of nanobands have been created. This work nicely demonstrates that the cyclic voltammetric response of a basal-plane HOPG electrode (BPPG) is solely due to the edge-plane defects present, no matter how small their coverage may be, and that the basal-plane graphite terraces have no influence on the voltammetry and are effectively inert; hence blocking the basal-plane sites results in no overall change to the observed voltammetry.

Last, it is important to note that researchers will (and have already done so) dispute the extensive literature reported above. As such it has been reported that under certain (limited) conditions the basal plane sites have measurable electrochemical activity [25–27]. Using elaborate Scanning Electrochemical Cell Microscopy (SECM) it has been reported that the basal plane sites of *freshly exposed* HOPG display considerable electroactivity which, interestingly, is time dependant, in that exposure to air for less than one hour after cleaving leads to a decrease in the observed electron transfer rates at the basal surface [27]. Such work is highly fascinating and studies into this time-dependent surface effect are, at the

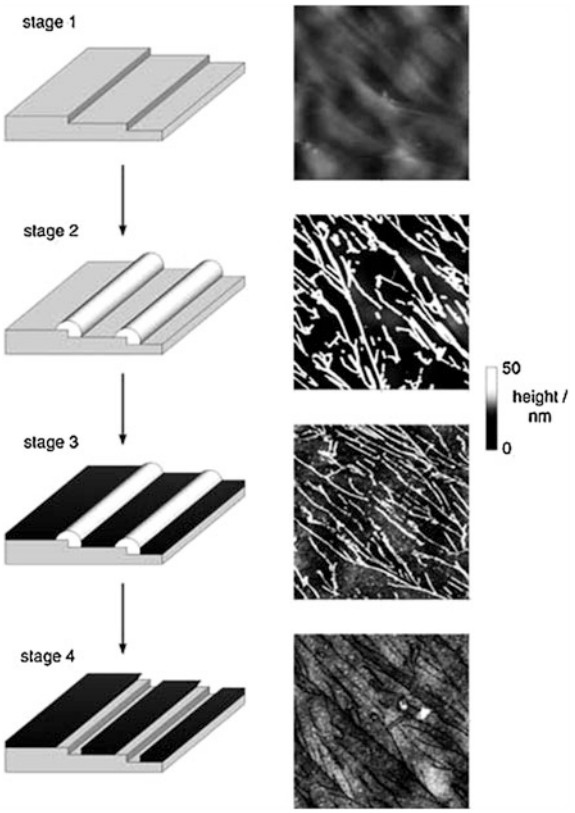

Fig. 3.10 Initially a HOPG surface is cleaved to produce a fresh surface (*stage 1*). In *stage 2*, MoO_2 nanowires are formed exclusively along the edge plane sites. In *stage 3*, the basal plane sites are covered by the electrochemical reduction of 4-nitrobenzenediazonium cations. *Stage 4* then involves exposing the edge plane sites by dissolution of MoO_2 in HCl. Reproduced from Ref. [4] with permission from Wiley

time of writing this *Handbook*, underway [27]. However, ultimately this means that over the lifetime of an experiment the observed electroactivity of the freshly cleaved basal plane sites of HOPG becomes negligible as previously reported [4–6]. Furthermore, an important challenge that has not been realised in Ref. [27] is the correlation of this local microscopic result to that of the well documented macroscopic response of a HOPG electrode; [28] i.e. if such 'pristine' HOPG surfaces, as used within Ref. [27], are used in a conventional cyclic voltammetric experiment, do the voltammograms appear fully reversible or not? If so can the pristine surfaces be reproduced by other groups? If not, then why not? [28].

3.2 Fundamental Electrochemistry of Graphene

When graphene is immobilised upon an electrode surface, as is common practice in the literature to electrically 'wire' (connect to) graphene and study its electrochemical activity, a heterogeneous electrode surface is formed. In this scenario, if we consider that a HOPG surface is utilised, Fig. 3.12 shows that four key sites

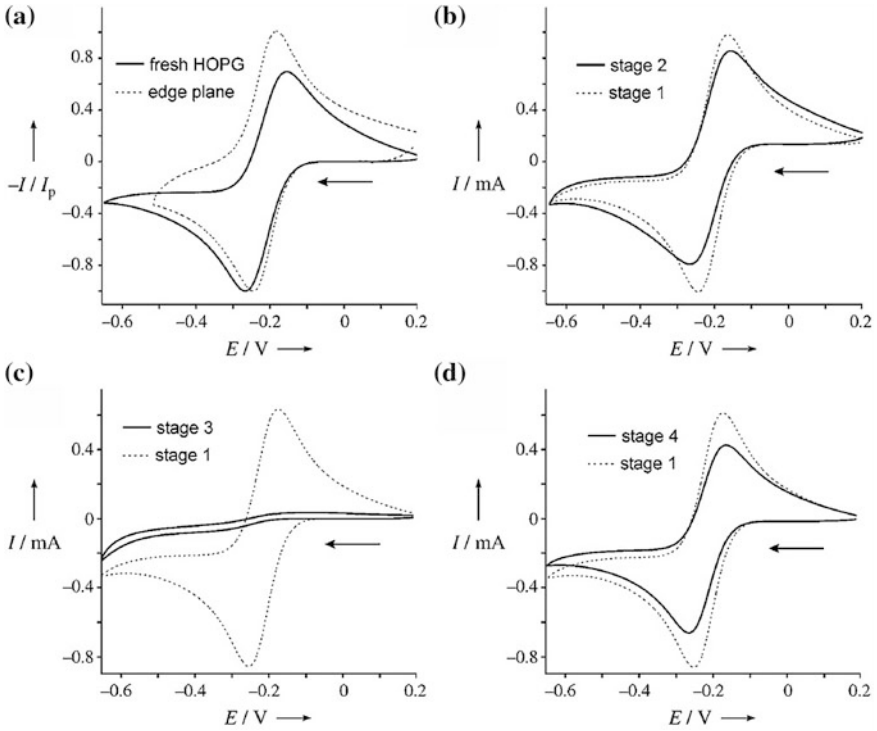

Fig. 3.11 Cyclic voltammograms for the reduction of 1.1 mM $[Ru(NH3)_6]^{3+}$ at a *HOPG* electrode (*vs*. SCE) after each stage of nanotrench fabrication (Fig. 3.10): **a** *stage 1*, **b** *stage 2*, **c** *stage 3*, **d** *stage 4*. The voltammograms in (**a**) were obtained from the same experiment with an EPPG electrode. Voltammograms in (**b**) through to (**d**) were obtained after *stage 1* of nanotrench fabrication. Reproduced from Ref. [4] with permission from Wiley

are evident. It is clear that in addition to the underlying HOPG electrode surface which has edge plane and basal plane sites, each with the their own electrochemical activity with different Butler-Volmer terms, k^o and α, the immobilisation of graphene with its own edge and basal plane sites (with their own k^o and α values) gives rise to an interesting situation. This scenario occurs when any carbon based electrode is utilised as the supporting electrode.

In the case of immobilising graphene upon a metallic electrode as is sometimes spuriously undertaken, such as a gold macroelectrode, there would be three key electrochemical sites, the underlying gold (k^o_{gold}, α_{gold}) and modified graphene with the contribution from edge and basal plane sites. However this is not a good situation as the underlying gold generally has (depending on the electroactive analyte) a greater electrochemical activity which dominates over the graphene (or other graphitic materials which could be employed) such that the contribution from graphene will not be solely observed or could be misinterpreted as graphene

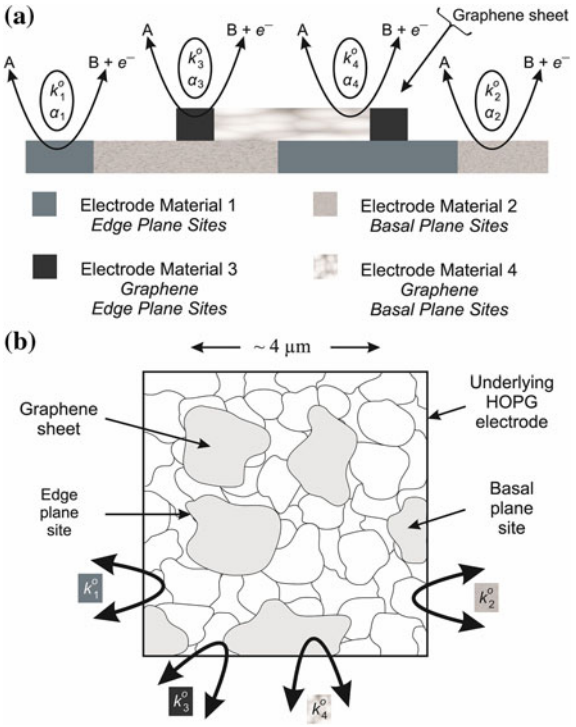

Fig. 3.12 **a** A schematic representation of an electrochemical reaction occurring on a graphene modified HOPG surface exhibiting differing Butler-Volmer characteristics; and a top-down perspective (**b**). Note that the figure is obviously not to scale

exhibiting excellent electrochemical activity if control experiments (bare/unmodified gold electrode) are not diligently undertaken.

Returning to the case of graphene as shown in Fig. 3.13 and utilising the insights discussed above from numerical simulations and experimental observations for graphitic electrodes (Sect. 3.1.2), *should graphene be considered similar to that of HOPG but as a single layer?* Given that graphite surfaces are heterogeneous (anisotropic) in nature, with the overall chemical and electrochemical reactivity differing greatly between two distinct structural contributions which are fundamental to the behaviour of graphitic electrodes, namely the edge and basal planes, graphene, a single layer that comprises HOPG, should in theory act similar in terms of its DOS to that observed for HOPG; Fig. 3.13 shows this concept.

If we assume that graphene is immobilised upon an electrode surface (and will naturally prefer to lie parallel rather than vertical due to π-π stacking) such that the underlying electrode is completely covered, we can approximate this graphene modified electrode surface to that shown in Fig. 3.6 where we have edge plane sites (viz the peripheral edge of graphene) and a basal plane (assuming for simplification that we have true graphene, that is pristine graphene with no defects across the basal surface), thus the same unit cell can be used and an approach can be taken via the diffusion domain method, which will be applicable, in that we have islands with nano edge bands of thickness which, at best, might approximate to the length of a carbon-carbon bond which is reported to be $\sim$0.142 nm in graphene. This can be

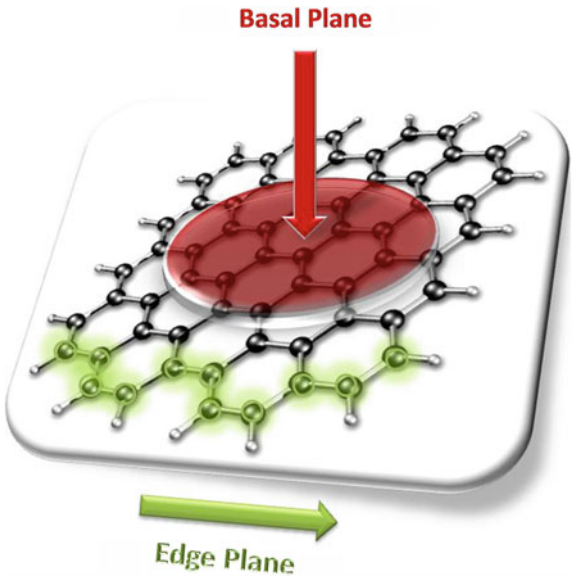

Fig. 3.13 A conceptual model depicting the structure of pristine graphene, showing the sites of electron transfer, basal and edge plane like- sites. Reproduced from Ref. [12] with permission from The Royal Society of Chemistry

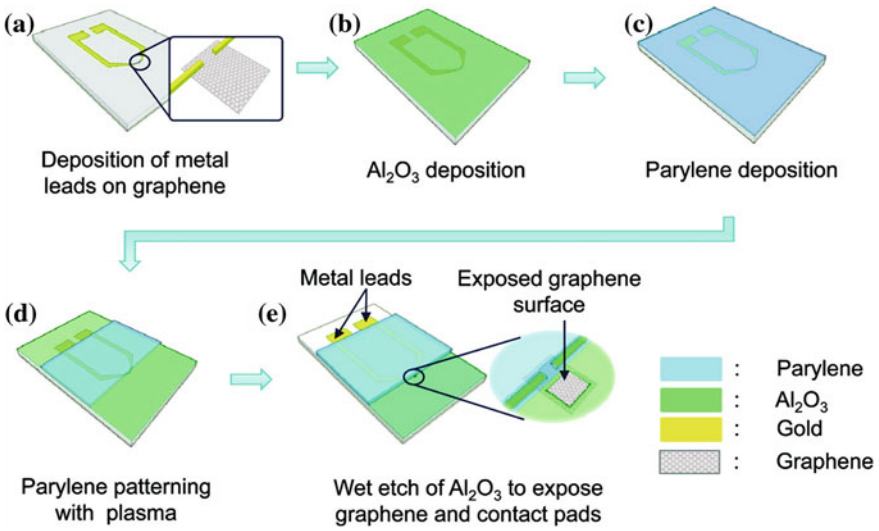

Fig. 3.14 Procedure for fabricating monolayer graphene sheets into working electrodes for electrochemical characterisation. Reprinted with permission from Ref. [29]. Copyright 2011 American Chemical Society

assumed to be constant in many different forms of graphene with the expectation that the domain radius changes (viz the L_a size) as the size of the graphene flake is either increased or decreased depending on its fabrication methodology.

If we consider two contrasting scenarios, assuming in the first instance that the edge plane has fast electron transfer activity and that the basal plane has some negligible activity ($\sim 10^{-9}$ cm s^{-1}), as is widely accepted in the case of HOPG and since graphene is simply one layer of this, the effect of the domain radius (L_a size) that will be expected can be observed from inspection of Fig. 3.7, showing that at a large domain radius two peaks might be observed. However, to date such voltammetric signatures have not yet been presented, adding weight to the inference that (as per the second scenario) the edge plane side of graphene is the electroactive site acting akin to an edge plane nano band; this is a reoccurring theme which we explore later with experimental evidence from throughout the literature. Thus in the case of modifying a HOPG surface with graphene, it is likely that the basal plane HOPG surface (BPPG), the k^o_{basal}, can be neglected such that Fig. 3.12 simplifies to two key domains, k^o_{edge} (HOPG) and k^o_{edge} (graphene), and assuming these are electrochemically similar in terms of the DOS, it is clear that edge plane sites are the key dominating factor of a graphene modified electrode.

3.2.1 Graphene as a Heterogeneous Electrode Surface

The electrochemistry of true graphene, that is, an individual monolayer crystal, has been reported by Li et al. [29] with their fabrication procedure overviewed in Fig. 3.14 where a monolayer graphene sheet is first deposited onto a SiO_2-coated Si substrate. In their study two types of graphene were explored, which were either fabricated via mechanical exfoliation (the so-called "scotch tape method" as covered in Chap. 1) or through CVD graphene growth. In both cases optical lithography was employed in order to be able to connect to each piece of graphene with two metal leads, as shown in Fig. 3.14a. Note that those working on the fabrication of graphene forget that one needs to somehow electrically wire and connect to the graphene sheet in order to utilise and study it!

In this work [29], after depositing the graphene sheet a 100 nm thick Al_2O_3 layer (see Fig. 3.14b), followed by a 600 nm thick parylene layer (see Fig. 3.14c), are deposited in order to isolate the metal leads from the solution such that when electrochemical experiments are performed the graphene response will be observed and the electrochemistry will not be dominated by the metal leads. This is achieved by employing an oxygen plasma to remove a region of the parylene layer above the graphene while keeping the metal leads covered (Fig. 3.14d). Finally, a window through the Al_2O_3 layer is made using a wet etch to expose a well-defined area of the graphene surface (Fig. 3.14e).

The elegant design of experimental set-up by Li et al. [29] ensures that graphene is the only electrochemically active surface that is in contact with the

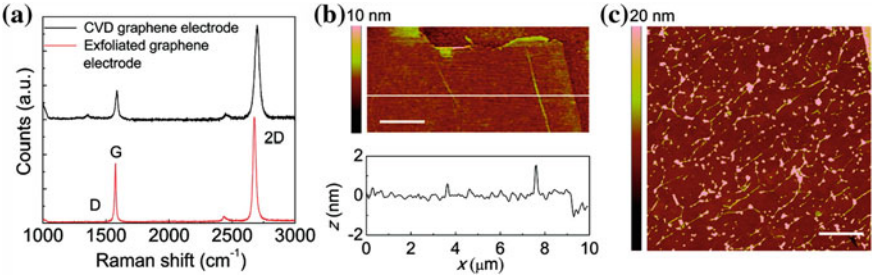

Fig. 3.15 Raman and AFM characterisation of the graphene working electrodes. **a** Raman spectra of the graphene working electrodes, after the device fabrication process was completed. **b** AFM image of the surface of a working electrode made of exfoliated graphene. A cross-sectional profile is given for the line in the top panel. Scale bar: 2 μm. **c** AFM image of the surface of a working electrode made of CVD graphene. Note that the entire area in (**c**) is within the surface of the CVD graphene electrode. Scale bar: 2 μm. Reprinted with permission from Ref. [29]. Copyright 2011 American Chemical Society

solution during electrochemical measurements. Additionally the fabrication steps were chosen to minimise the likelihood of contaminating the graphene. The maximum sizes of the exposed graphene surfaces were reported to be 15×15 μm^2 for the mechanically exfoliated graphene and 0.38×0.50 mm^2 for the CVD grown graphene since CVD graphene can be formed in much larger sheets than exfoliated graphene. In the final step, vacuum annealing at 350 °C was used in an attempt to remove organic residuals which might have remained on the graphene surface after processing [29].

Figure 3.15 shows Raman and AFM characterisation of the fabricated graphene electrodes where a symmetric single peak is observed for the 2D band, the intensity of which is significantly higher than that of the G peak confirming that high-quality single graphene layers have been obtained from the fabrication methodologies. Additionally note that a small D peak is also observed (for CVD) indicating a less pristine layer, as is generally the case for such samples. Electrodes made via this route were found to be more disordered including large wrinkles, particulates, and domain-like structures following the CVD growth and transfer process (Fig. 3.15c). For electrodes made via mechanical exfoliation (in this case), no observable D peak was evident at 1,350 cm^{-1}, indicating that the graphene sheet is clean and (at the resolution limit of micro-Raman) defect-free [29]. The step height of the graphene layer with respect to the SiO_2 substrate was $\sim$0.8 nm, in good agreement with the known value for clean graphene (0.5–1 nm).

Electrochemical experiments revealed a microelectrode response (steady-state current; see Chap. 2) at both the graphene electrodes, with the effective area of the graphene electrode deduced from the following equation [29]:

$$A_{eff} = \pi \left(\frac{i_{ss}}{4nFDC} \right)^2 \tag{3.6}$$

where A_{eff} is the effective area of the microelectrode/graphene electrode and i_{ss} is the steady-state current. The A_{eff} of the graphene electrodes was estimated to correspond to $117 \pm 8\ \mu m^2$, which is in good agreement with Atomic Force Microscopy (AFM) (found to correspond to $\sim 130\ \mu m^2$). [29] The standard electrochemical rate constant was deduced for FcMeOH to be $\sim 0.5\ cm\ s^{-1}$ indicating an electrode with fast electron transfer kinetics [29]. The authors' infer that improvements in the electron transfer kinetics (observed when contrasted to the basal plane of HOPG) are due to corrugations in the graphene sheet, [29] or could arise from edge plane like- sites/defects across the basal plane surface of the graphene in addition to exposed edges acting like ultra-microelectrodes, with the sigmoidal voltammetry arising from the change in mass transport—the observations and inferences are highly fascinating, indicating why graphene is being fundamentally studied.

The electrochemistry of individual single and double layered graphene crystals has also been reported by Dryfe and co-workers [30] who performed time consuming experiments producing single mono-, bi- and multi- layer graphene crystals viz mechanical exfoliation ('scotch tape method') after which the authors electrically connected their graphene samples and encapsulated them with epoxy such that only the basal plane site (side) of graphene was exposed to the solution [30]. Optical images of the graphene and prepared graphene electrodes are shown in Fig. 3.16.

As shown in Fig. 3.17 (depicting the current response for the case of mono-, bi- and multi-layer graphene), sigmoidal currents were observed using the potassium ferri-/ferro- cyanide redox probe due to the exposed graphene surface effectively being a large microelectrode [30]; Chap. 2 overviews how changes in the electrode geometry can give rise to different mass transport and hence different voltammetric signatures.

Given that the edge of the graphene is covered with insulating epoxy and only its basal plane sites are exposed, it is surprising to observe any voltammetry at all. The reason for this observed voltammetry is that defects across the graphene surface reside [30], where there is a missing lattice atom and as such a dangling bond is exposed providing electrochemically reactive sites. Figure 3.18 shows a typical defect observed in graphene with TEM, Density Functional Theory (DFT) simulation of a graphene defect and an experimentally observed defect via STM [31]. Note also that the effect of defects on HOPG is well known, in that a 1 % defect density is estimated to result in a 10^3 factor increase in the heterogeneous electron transfer rate constant [32]. Dryfe et al. demonstrate that while their graphene surface has a low level of defects, fast electron transfer is observed due to the defects that are present on the graphene surface [30] and resultantly a similar voltammetric response is observed at bi-layer graphene (see Fig. 3.17) due to the top graphene layer only being exposed. Such work indicates that surface defects are extremely important in obtaining fast electron transfer rates, which has been shown for pristine graphene (see later) [33].

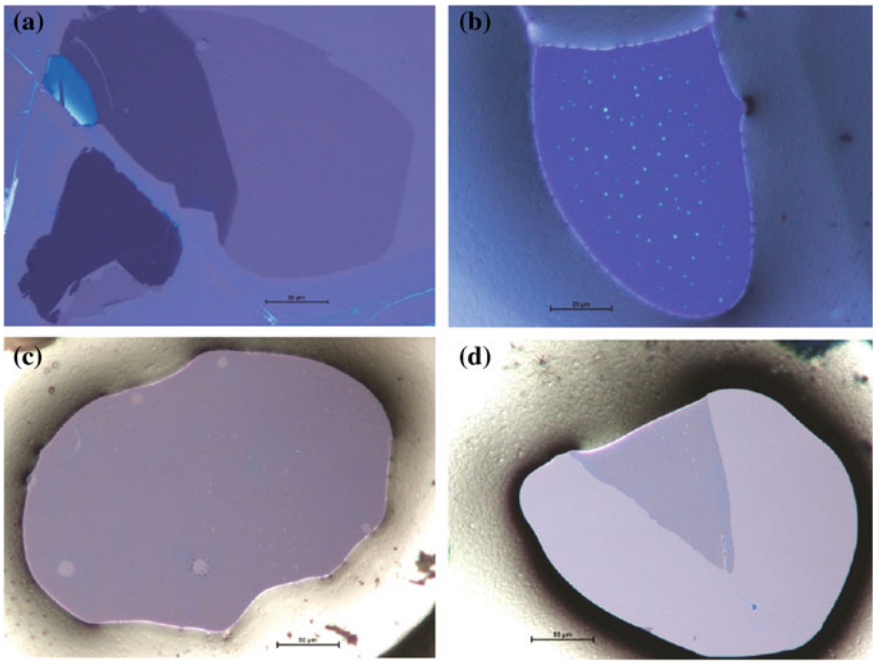

Fig. 3.16 Optical micrographs of monolayer graphene samples. Sample 1 is shown *before* (**a**) and *after* (**b**) masking; in image (**b**) edges are completely masked. Sample 2 is shown to contain holes in panel (**c**); in panel (**d**) the exposed part of sample 3 is *triangular*, hence edges are exposed to the solution. Details of each sample can be found in the legend of Fig. 3.17. *Scale bars*; (**a**, **c** and **d**) 50 μm and (**c**) 20 μm. Reprinted with permission from Ref. [30]. Copyright 2011 American Chemical Society

In the work of Dryfe [30], defects across the surface of the graphene are most probably due to the mechanical stresses involved in obtaining graphene from graphite using the 'scotch tape' (mechanical exfoliation) method. The sigmoidal response is likely due to the small size of the graphene sheet acting like a microelectrode (see Fig. 3.17) which is complicated further if the graphene is recessed by the epoxy. Note that defects across the basal surface of graphene are hard to determine and one approach is to use TEM and Scanning Tunnelling Microscopy (STM). Figure 3.18 shows a TEM image of a defect in graphene along with simulated structures and a STM image of a single vacancy; clearly determining defects is a challenging task.

The above reports are currently, at the time of writing this *Handbook*, the only two examples in the literature where individual graphene crystals have been electrochemically probed on the micro-scale and the reason as to why this is, is due to the large amount of effort that one has to undertake in order to perform such experiments. Clearly these are fundamental studies with the fabrication not scalable such that the most common approach to utilise graphene is to immobilise it

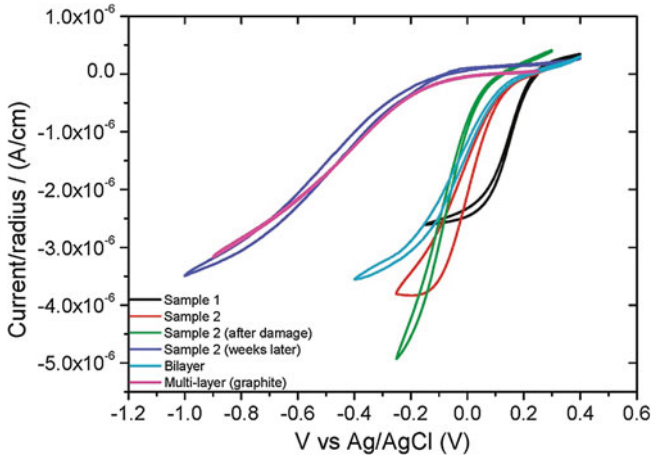

Fig. 3.17 Ferricyanide voltammetry: Current (normalised to electrode radius) versus potential response for the graphene monolayer samples (Samples 1 and 2: 1, monolayer contained no visible defects and its edges were completely masked—note however that although special attention was paid during the masking and preparation of samples in order to expose areas with the minimum number of defects, the authors acknowledge that to date it has not been possible to achieve a perfect, edge-free region; 2, monolayer contains several holes of $\sim$10 μm diameter, hence some edge sites must be in contact with the electrolyte), a bilayer sample and the multilayer sample. Scan rate = 5 mVs^{-1}; concentration = 1 mM ferricyanide in 1 M KCl. Reprinted with permission from Ref. [30]. Copyright 2011 American Chemical Society

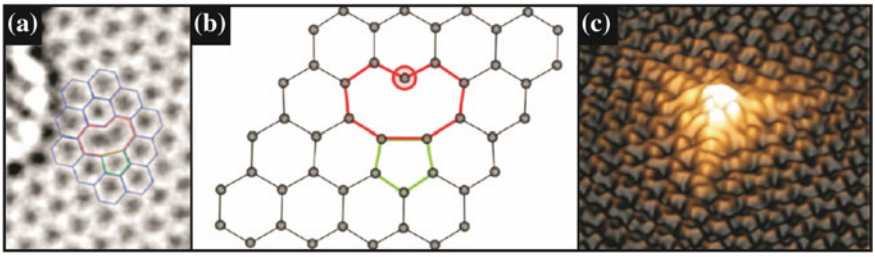

Fig. 3.18 **a** TEM image of a defect in a graphene lattice (Reprinted with permission from Ref. [34]. Copyright 2008 American Chemical Society); **b** Simulated atomic structure obtained via DFT calculations (Reprinted with permission from Ref. [31]. Copyright 2010 American Chemical Society); **c** An experimental STM image of a single vacancy, appearing as a protrusion due to an increase in the local DOS at the dangling bond (marked with a circle in *panel b*) (Reprinted with permission from Ref. [35]. Copyright 2010 The American Physical Society)

upon a suitable electrode surface such that one is effectively averaging a response over that of the graphene domains.

Key insights into the electrochemical reactivity of pristine graphene have been provided [33] through the modification of edge plane- and basal plane- pyrolytic graphite (EPPG and BPPG respectively) electrodes with pristine graphene, as is

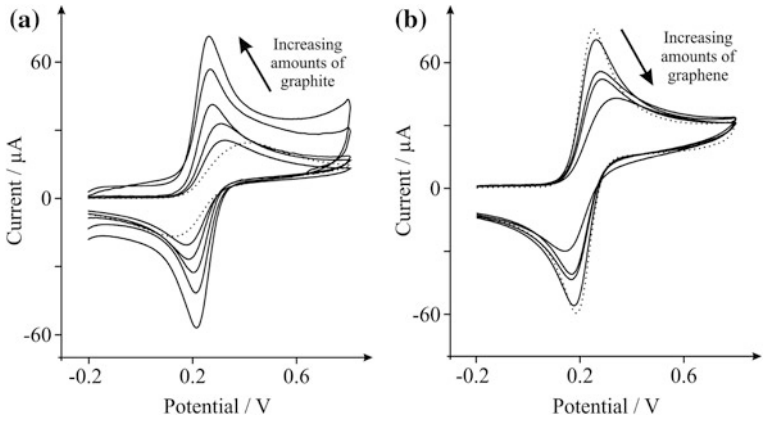

Fig. 3.19 Cyclic voltammetric profiles recorded utilising 1 mM potassium ferrocyanide(II) in 1 M KCl. **a** obtained using a BPPG electrode (*dotted line*) with the addition of increasing amounts of 2, 4, 50, 100, and 200 µg graphite (*solid lines*). **b** obtained using an EPPG electrode (*dotted line*) with the addition of increasing amounts of 10, 20, 30, and 40 ng graphene (*solid lines*). Scan rate: 100 mVs^{-1} (*vs.* SCE). Reproduced from Ref. [33] with permission from The Royal Society of Chemistry

common place in the literature in order to 'electrically wire' and connect to the graphene under investigation. The authors utilised a plethora of electroactive probes that have been commonly employed within the field (are well characterised on graphitic materials) and consequently have been well understood over many decades. Surprisingly, such work was the first to show a deviation from the wealth of literature on graphene at that time, in that pristine graphene was shown not to be as beneficial as previously reported [33].

Due to the type of graphene utilised, that is, high quality graphene with a low density of defects across the basal plane surface of the graphene sheet as well as a low oxygen content, it was observed that graphene exhibits slow electron transfer kinetics and as a result the electrochemical response (of the supported graphene layer) was found to actually block the underlying electrode surface [33]. The observed voltammetric response is presented in Fig. 3.19 for the electrochemical oxidation of ferrocyanide. Shown in Fig. 3.19a is the response of a BPPG electrode following modification with graphite, where it is well known that graphite has a large proportion of edge plane like- sites/defects and hence when one immobilises the graphite, the underlying electrode surface which exhibited slow electron transfer (note the large peak-to-peak separation, ΔE_P) exhibits a change (improvement) in the voltammetric signature due to the surface becoming populated with edge plane sites. In the case of graphene however (Fig. 3.19b), the reverse is observed, that is the introduction of graphene appears to be blocking the underlying electrode surface. In this case, when graphene was introduced onto a surface that exhibited fast electron transfer rates and a high degree of edge plane sites (an EPPG electrode), the immobilised graphene blocked the fast electron

transfer occurring at the underlying surface, reducing the overall electrochemical activity, which can be attributed via the fundamental knowledge on graphite electrodes (see Sect. 3.1.2) to be due to the high proportion of relatively inert basal plane surface on pristine graphene as opposed to a small structural contribution from edge plane sites/defects [33].

In terms of the coverage of graphene over a supporting substrate, a key experimental parameter that needs to be considered, it was indicated that two "working zones" will arise when researchers immobilise graphene upon electrode substrates [33]. The first zone, '*Zone I*' corresponds to the modification of the electrode surface resulting in single- and few-layer graphene modified electrodes, which block the electrochemical response observed at the underlying electrode. Upon increasing amounts of graphene, the underlying electrode is continuing to be blocked (as shown in Fig. 3.19b). This is since the material (graphene) that is being immobilised has a low proportion of edge plane sites since the proportion of edge plane sites to basal plane sites (within its geometric structure) are extremely low and given its pristine nature, edge plane sites/defects across the basal surface are negligible. Upon the addition of more graphene, a '*Zone II*' becomes evident [33]. This is where several/significant layers of graphene are observed (viz *quasi*-graphene [36] and graphite) which leads to an increment in the density of edge plane sites (due to its geometric structure) and thus improved voltammetry via increased heterogeneous electron transfer rates (as is evident in Fig. 3.19a). This response continues until a limit is observed, typically from the instability of the graphene upon the underlying electrode surface/support. Clearly the coverage of graphene is a key parameter in graphene electrochemistry, where the incorrect use/characterisation of a graphene modified surface could mislead those that are actually observing graphite (but believe they are using graphene) into misreporting the benefits of graphene, i.e. if working in *Zone II*. Note that recently a '*Zone III*' has been shown to exist in that, when excessive amounts of graphene is immobilised thin-layer effects dominate, giving the false impression of electro-catalysis; Chap. 2 overviews this concept.

Figure 3.20 highlights the change in the structure of the electrode surface from introducing graphene and the resultant electrochemical responses expected. Figure 3.20a shows a cyclic voltammetric profile as typically observed at an edge plane HOPG electrode assumed to possess fast electron transfer kinetics and following the immobilisation of single-layer graphene (Fig. 3.20b) where an incomplete coverage of the surface is realised. Effectively one is replacing a highly efficient and electrochemically reactive surface with graphene which has a low proportion of edge plane sites and no defects across the basal plane surface of the graphene, giving rise to the observed voltammetry with an increased ΔE_P indicating a departure towards slower electron transfer kinetics [33]. Following complete single-layer coverage (Fig. 3.20c) of graphene the ΔE_P increases which is firmly in *Zone I* as identified above. As more graphene is immobilised (Fig. 3.20d), a departure from single-layer, or approximate single layer/double and few layer (*quasi*-graphene) [36] is evident to that of multi-layer graphene (viz graphite) where one is now in *Zone II*, such that the voltammetric response heads

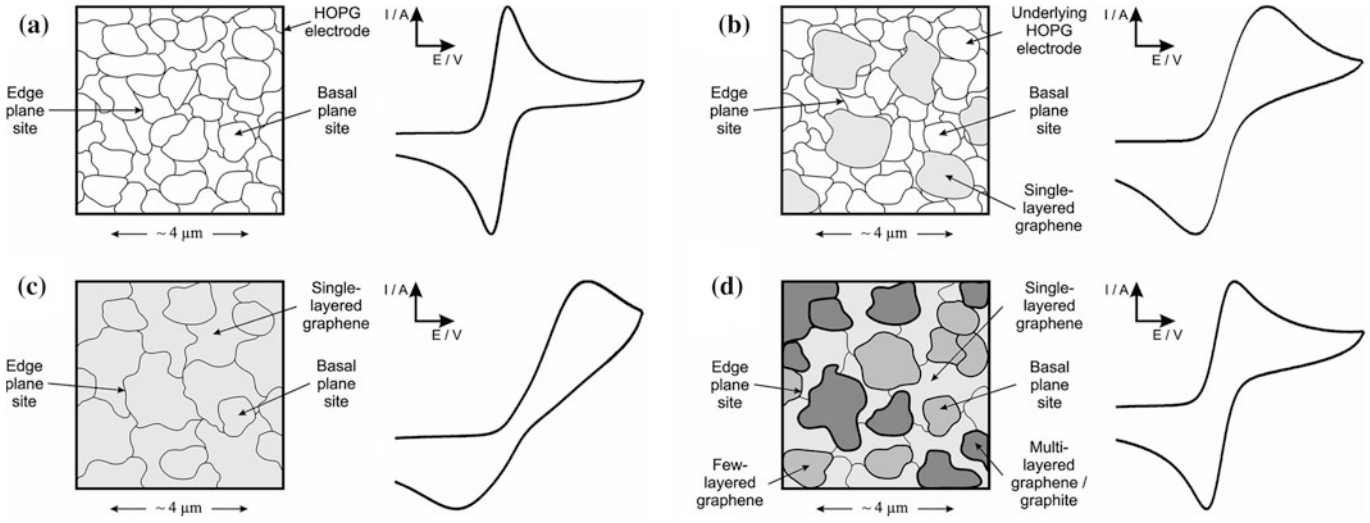

Fig. 3.20 Schematic representation of the effect on the cyclic voltammetric profiles that will be observed for a *HOPG* electrode following modification with differing coverages of graphene using a simple outer-sphere electron transfer redox probe. **a** Represents an unmodified *HOPG* electrode surface where fast electron transfer kinetics are observable **b** after modification with graphene leading to incomplete coverage where reduced electron transfer rates occur **c** after modification with graphene leading to complete single layer coverage where due to the large basal content of graphene (with little edge plane contribution) poor electrochemical activity is observed where electron transfer is effectively blocked, and **d** after continual modification with graphene leading to layered structures with increased edge plane sites available (origin of fast electron transfer) and thus an improvement in the electrochemical response is observed. Reproduced from Ref. [33] with permission from The Royal Society of Chemistry

back towards that originally observed for HOPG (Fig. 3.20a) due to the now large proportion of edge plane sites upon the electrode surface [33].

Thus, Brownson et al. has shown that given the geometric structure of graphite (multiple layers of stacked graphene), by its very nature it possesses a larger proportion of edge plane sites than that of single layer graphene and thus the former exhibits improved electrochemical activity, heterogeneous electron transfer kinetics, over that of the latter [33].

Returning to the case of immobilising pristine graphene onto a HOPG surface for electrochemical investigation (see above), insights from Brownson et al. [33] reveal that the underlying (supporting) electrode surface plays an important role, as does the orientation of the immobilised graphene. SEM images in the above work revealed that coalesced graphene 'folds' over edge plane sites of the underlying electrode, potentially explaining the blocking effect observed when graphene is introduced. Upon further additions of graphene, orientation with the edge plane sites of the underlying electrode results in a vertically aligned or disorder graphene surface and hence a beneficial increase in the electrochemical response is observed due to the increment in the proportion of edge plane sites accessible for electron transfer [33]. In this model it is assumed that the immobilised graphene adopts a similar architecture to that of the underlying electrode since the graphene has a distributed electron density of the planar–basal site (π–π) which will be disturbed by the high electron density of the underlying edge sites of the graphene (the EPPG) such that it effectively 'aligns' with the underlying electrode surface as this arrangement reflects the lowest energy settlement [33]. Due to the high number of graphene sheets on the EPPG electrode the graphene sheets will stack (as a continuation of the edge planes) in parallel to each other in order to fit the limited space of the EPPG surface. In the case of graphene upon a BPPG electrode surface the graphene will follow the same architecture as presented by the BPPG sheets, meaning that the graphene will stack planar on the BPPG due to π–π stacking: Fig. 3.21 depicts SEM images showing this concept.

Last, insights from DFT simulations on different sizes of graphene reveal a greater electron density at the edge of pristine graphene which confirms the observations by Brownson et al. [33] and in other work [37, 38] such that, similar to that observed for HOPG, the peripheral edge of graphene as opposed to its side acts electrochemically akin to that of edge plane sites and the latter to that of basal plane sites; in this case pristine graphene assumes no defects (defect sites, missing atoms, dangling bonds etc.) across the surface of the graphene, the introduction of which will beneficially contribute to the electrochemical activity of graphene. Note that in the case of graphite a greater density of edge plane sites is well known to result in an improved electrochemical reactivity [1, 4–6]; but until the above reports this was lesser reported for graphene.

In support of the above work it has been shown, using SECM to study correlations in monolayer and multilayer graphene electrodes grown via CVD, that in terms of these layered structures, single layer graphene exhibits the lowest electrochemical activity and that activity increases systematically when increasing the number of graphene layers, to a situation where the flakes are so active that the

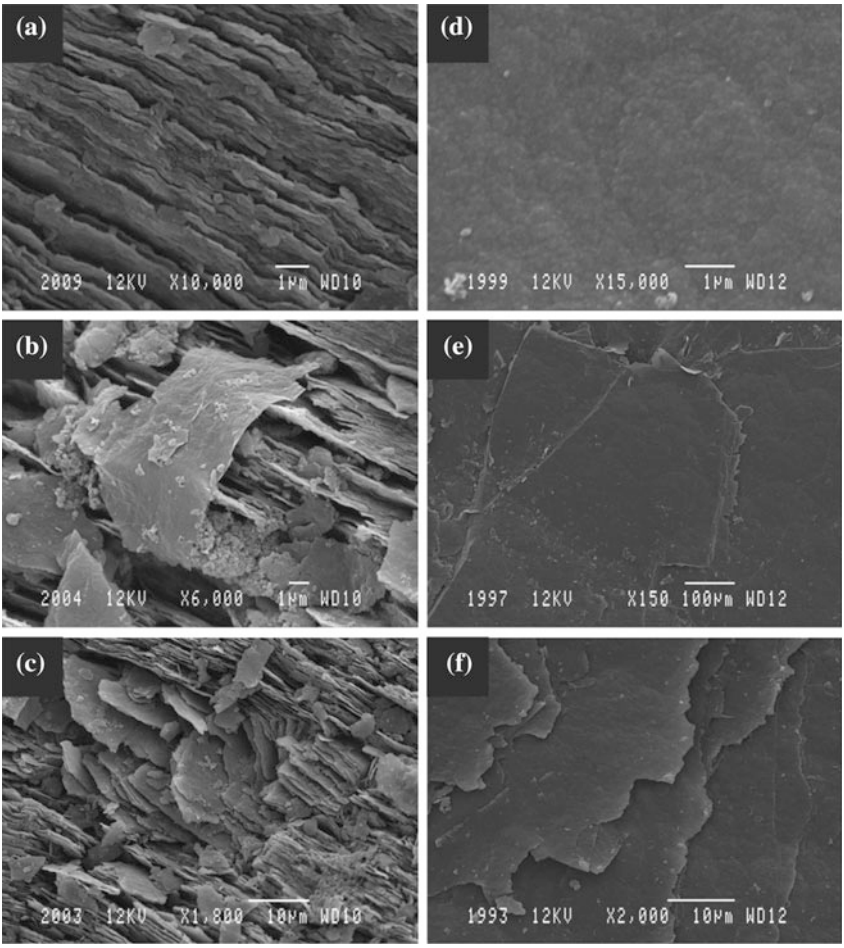

Fig. 3.21 SEM images of an unpolished EPPG electrode before (**a**) and after modification with low (**b**) and high (**c**) coverage's of graphene, and additionally an unpolished BPPG electrode before (**d**) and after modification with low (**e**) and high (**f**) coverage's of graphene. Reproduced from Ref. [33] with permission from The Royal Society of Chemistry

electron transfer process becomes nearly electrochemically reversible at greater than 7 layers (viz graphite) [39]. Figure 3.22 shows the electrochemical current as a function of increasing graphene layers using SECM which shows that single layer graphene exhibits the lowest electrochemical activity [39]. Such work confirms the work of Brownson et al., that states 'single layer (and bi- and few- layer (*quasi*-graphene)) graphene is not such a beneficial electrode material (when contrasted to graphite in terms of the heterogeneous electron transfer kinetics) and that in fact, in cases where beneficial electron kinetics are reported at graphene, it is likely that researchers are putting large quantities of graphene upon their electrode surfaces such that there is a large deviation from graphene to that of

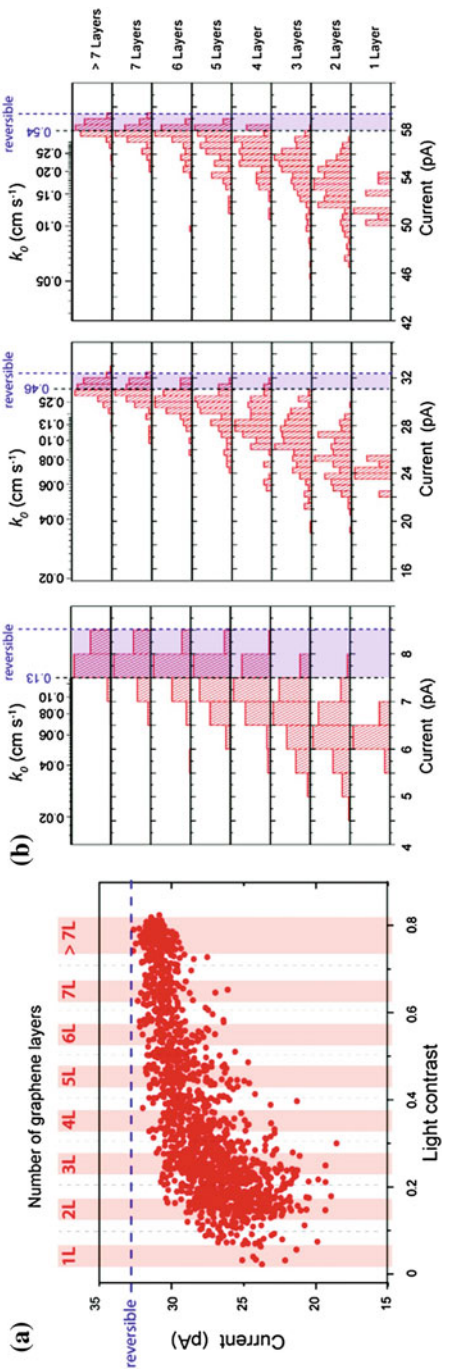

Fig. 3.22 **a** Pixel-by-pixel correlation between the electrochemical current map at potential E_2 and the number of graphene layers. **b** Histograms of the electrochemical current and standard rate constant, k^0, for each defined number of CVD graphene layers, for potentials E_1, E_2, and E_3 (from left to right). The electrochemical oxidation of 2 mM $FcTMA^+$ (30 mM KCl) is used as the voltammetric probe with E_1, E_2, and E_3 corresponding to points on the voltammetric response of the $FcTMA^+$. The *dashed line* in (**a**) and the *blue* area in (**b**) denote the conditions where the electron transfer process becomes entirely reversible. Reprinted with permission from Ref. [39]. Copyright 2012 American Chemical Society

graphite and thus false claims of improvements in the electrochemical processes of graphene are generally reported (which should instead be attributed to graphite and/or other graphitic structures).

Other notable work adding to the fundamental understanding of graphene is by Lim et al. [40], who investigated the effect of edge plane defects on the heterogeneous charge transfer kinetics and capacitive noise at the basal plane of CVD fabricated epitaxial graphene (prepared on a silicon carbide substrate) using inner-sphere and outer-sphere redox mediators. The authors showed that the basal plane surface of graphene exhibits slow heterogeneous electron transfer kinetics, interestingly however, when electrochemically anodised (increasing the degree of oxygen-related edge plane defects) they found that the defects created on its surface resulted in the improvements of election transfer rates that surpass those observed for pristine graphene, Glassy Carbon (GC) and Boron Doped Diamond (BDD) electrodes [40]. Again, this work confirms the essential need for edge plane like-sites/defects on the surface of graphene (for improved electrochemical reactivity). Note, it is well known that the presence of oxygen related species on a carbon based electrode material can dramatically influence the observed electrochemical reactivity, either beneficially or detrimentally depending on the target analyte [2, 41–45]. Thus it could be inferred that the oxygen-related species purposely introduced onto the graphene surface in this case contribute to a hidden origin of the improved rate kinetics. However, this is not the case and the contribution from the oxygenated species residing on the graphene can be neglected since the authors utilised a range of electro-active species to study their graphene, ranging from simple outer-sphere electron transfer probes to surface sensitive inner-sphere species (see Box 3.1), and the observed trend was similar for all compounds.

BOX 3.1: Surface Sensitivity at Inner- and Outer- Sphere Redox Probes

A common approach within electrochemical studies in order to greater understand the material under investigation is the utilisation of inner-sphere and outer-sphere redox mediators/probes. Such electron transfer processes differ significantly according to the 'sensitivity' of their electron transfer kinetics to the surface chemistry of the carbon electrode/material under investigation in terms of the surface structure/cleanliness (defects, impurities or adsorption sites) and the absence/presence of specific oxygen containing functionalities, that is, variations in k^o with the condition of the electrode surface [1, 46].

Outer-sphere redox mediators (see Fig. 3.23 for examples) are termed *surface insensitive* such that k^o is not influenced by the surface oxygen-carbon ratio, surface state/cleanliness in terms of a surface coating of a monolayer film of uncharged adsorbates, or specific adsorption to surface groups/sites [1]. There is no chemical interaction or catalytic mechanism involving interaction (i.e. an adsorption step)

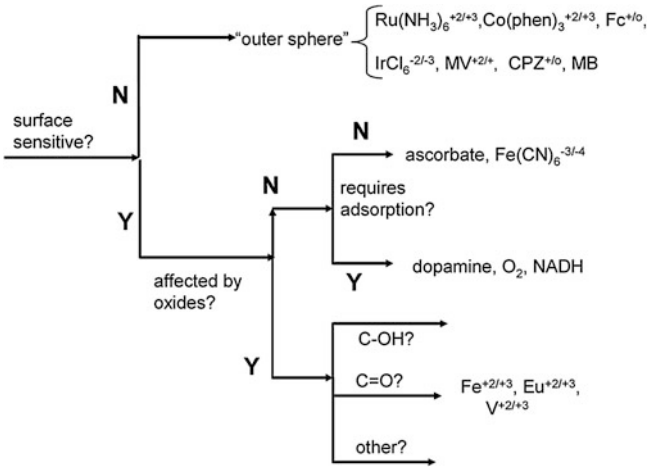

Fig. 3.23 Classification of redox systems according to their kinetic sensitivity to particular surface modifications on carbon electrodes. Reprinted with permission from Ref. [47]. Copyright 1995 American Chemical Society

with the surface or a surface group—such systems often have low reorganisation energies [1, 46]; in this case the electrode merely serves as a source (or sink) of electrons and as such outer-sphere systems are sensitive primarily to the electronic structure due to the electronic DOS of the electrode material [1, 46].

Inner-sphere redox mediators (see Fig. 3.23 for examples) are termed *surface sensitive* in that the k^o is strongly influenced by the state of the electrode surface (surface chemistry and microstructure) via specific electro-catalytic interactions that are inhibited significantly if the surface is obscured by adsorbates (or impurities). Such interactions can also depend strongly on the presence (or absence) of specific oxygenated species which give rise to either beneficial or detrimental effects [1, 46]. In this case systems are more largely affected by surface state/structure and/or require a specific surface interaction, being catalysed (or inhibited) by specific interactions with surface functional groups (adsorption sites) rather than the DOS as such systems generally have high reorganisation energies [1, 46].

The observation of differing responses when using varied inner- and outer- sphere redox probes allows insights to be deduced regarding the state of the surface structure of the electrode material in question. McCreery [62, 87] has provided a "road map" for commonly utilised redox probes, as shown in Fig. 3.23, which allows researchers to clarify from experimental observations the redox systems and how they are affected.

Other notable work that supports the findings that edge plane sites of graphene are dominantly reactive over that of its basal plane has been published by Keeley et al. [48, 49], in which the authors sonicated graphite powder in dimethylformamide for 72 h in order to achieve exfoliation of graphene nanosheets whilst precluding the need for chemical oxidation and as such alleviating any unnecessary contributions from the presence of surface oxygenated species. TEM analysis showed that 90 % of the resultant nanosheets contained five or fewer graphene layers and the lateral dimensions were mostly less than 1 μm, leading to a much higher density of edge plane- like sites than the parent graphite, as was confirmed by Raman spectroscopy. Cyclic voltammetric measurements with common redox probes confirmed that nanosheet-functionalised electrodes had larger active areas and exhibited far more rapid electron transfer than the plain/unmodified electrodes. Due to the absence of oxygen-containing groups in the solvent-exfoliated graphene, the observed electrochemical activity was attributed to originate from the numerous edge plane- like sites and defects on the graphene nanosheets [48, 49]. Moreover, other work has considered the electrochemical activities of open and folded graphene edges (in which the folded edges were structurally more similar to basal plane) where it was demonstrated that the heterogeneous electron transfer rate is significantly lower on folded graphene edges than that of open graphene edges (as is evident in Fig. 3.24 where larger ΔE_P is observed at the former over that of the latter) [50]; again such work concurs with the concept that the edge plane of graphene is the origin of electron transfer [33]. It is clear that there is a requirement to have exposed edges of graphene to achieve optimal electrochemical activity (fast electron transfer rates), or equivalently to have a high density of edge plane like- sites/defects across the graphene surface.

As highlighted in Chap. 1 different preparative methods of graphene result in structures that have greatly varied densities of edge plane defects [12] and thus it has been shown that the method of graphene preparation consequently has a dramatic influence on the materials properties and electrochemical reactivity [12, 51]. Furthermore, surface defects can be selectively introduced into the graphene structure post-synthesis, for example through the use of ion or electron irradiation, selective oxidation (with optional reduction), or by mechanical damage [31]. Note that incorporation of dopants/foreign atoms (i.e. nitrogen doping, see later) or the introduction of functionalities (i.e. oxygenated species) in addition to the formation of composite (or novel three-dimensional) [36] graphene based materials have also all been reported to alter the electrochemical properties of graphene either beneficially or detrimentally, that is, in terms of the observed heterogeneous electron transfer rates, DOS, intrinsic catalytic attributes and influences on surface adsorption/desorption processes (see Chap. 4 for examples of how this can be utilised to result in beneficial performances being observed at modified graphenes for various applications) [20, 41–45, 52, 53]. Importantly, if controllable and reproducible defect densities of graphene can be achieved and quantified [38], as has been shown to be the case at CVD graphene [12], then the electrochemical reactivity of graphene can be optimised and efficiently tailored when designing

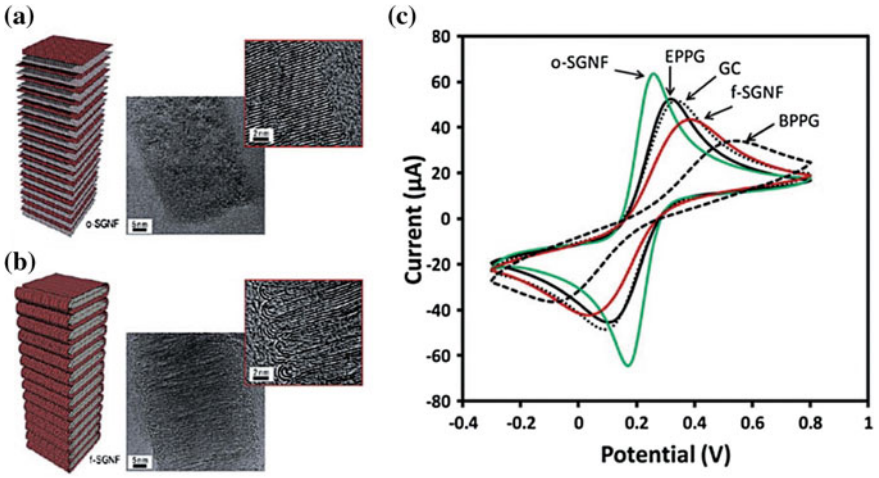

Fig. 3.24 Electrochemistry at folded edges of graphene sheets. Schematic drawing and TEM micrographs of **a** open and **b** folded graphene edge nanostructures. The drawing is not to scale and it should be noted that the "opening" of the folded edge nanostructure is to illustrate the inner structure of the fibre. The structural difference between open (**a**) and folded (**b**) edges are clearly visible in the detailed TEM images on the right (Note, scale bars represent 5 and 2 nm in each case). (**c**) Cyclic voltammograms of 5 mM potassium ferrocyanide(II) in 0.1 M KCl supporting electrolyte on open graphene structure (*green*; *o-SGNF*), folded graphene structure (*red*; *f-SGNF*), *EPPG* (*solid line*), *GC* (*dotted line*) and *BPPG* (*dashed line*) electrodes. Scan rate 100 mVs^{-1} (*vs.* Ag/AgCl reference electrode). Reproduced from Ref. [50] with permission from The Royal Society of Chemistry

graphene based devices with dedicated properties to achieve new functions/applications (to exhibit either fast or slow heterogeneous electron transfer—or to possess specific binding/attachment sites in the case of functionalisation). Thus effectively graphene can provide an electrochemically beneficial platform where it is possible to modify the graphene structure so that the properties of this material suit specific needs; such tailoring and versatility is of eminent importance for practical applications as well as for academic research.

3.2.2 Effect of Surfactants on the Electrochemistry of Graphene

As highlighted in Sect. 1.2 suspensions of graphene in a liquid are often (but not always) stabilised by surfactants, which are routinely incorporated into the fabrication of commercially available graphene to reduce the likelihood of the graphene sheets coalescing. When this is the case a tentative approach must be employed when utilising such graphene solutions within electrochemistry [54–57]. It has been established that some surfactants [58], for example sodium cholate [54–57],

exhibit measurable electrochemical activity and can thus contribute towards or even dominate the electrochemical properties and performance of the stabilised graphene, such that highly negative effects on the interpretation of data have been observed [54–57]. This was demonstrated to be the case towards the detection of β-nicotinamide adenine dinucleotide (NADH) and acetaminophen (APAP; paracetamol) as well as in the stripping voltammetry of heavy metals [54, 55]. These interferences/effects also extended to energy storage applications where it was demonstrated that surfactants themselves provide a higher capacitance than graphene, thus one must be cautious when attributing beneficial effects to graphene in these instances [57].

This work poses a highly important warning to the graphene community to always consider the effect/influence of any surfactant/solvent that is used to aid graphene dispersion. It is clear that appropriate control experiments need to be employed before the beneficial electrochemistry of graphene can be correctly reported and such control measures are thus required in future experiments in order to sufficiently de-convolute the true performance of graphene. Such a warning can be extended to other aspects of graphene electrochemistry, including the requirement for appropriate control and comparison experiments when determining the contribution to the electrochemical response of graphene in terms of the presence of graphitic impurities and oxygenated species (see Chap. 4).

3.2.3 Metallic and Carbonaceous Impurities on the Electrochemistry of Graphene

When carbon nanotubes (CNTs, which are effectively rolled up graphene structures) were first utilised in electrochemical applications they were found to contain metallic impurities as a result of their CVD fabrication, which contributed or dominated their observed electrochemical response [59, 60]. Similarly, it has been shown that graphene fabricated from graphite, via chemical oxidation of natural graphite followed with thermal exfoliation/reduction, can contain cobalt, copper, iron, molybdenum and nickel oxide particles which can influence the electrochemistry of graphene towards specific analytes and has potential to lead to inaccurate claims of the electro-catalytic effect of graphene [61, 62].

Note that such impurities (as noted above) can be avoided since, in the methodology, the grade of graphite purchased will largely dictate the final product and the highest purity graphite should be used (as well as high purity aqueous and non-aqueous solvents) to alleviate such problems. Nonetheless, as with Sects. 3.2.2 and 3.2.6 this valuable work highlights the importance of sufficient control experimentation when exploring graphene within electrochemistry. Note also however, that in certain cases the presence of metallic impurities may be beneficial with respect to the observed electrochemical response and thus indeed purposely incorporated as part of the fabrication process with the aim of producing noble

metal (Pd, Ru, Rh, Pt, Au or Ag) doped/decorated graphene hybrid structures that exhibit beneficial electronic properties, for use in electrocatalytic sensing for example [63]; nevertheless, in such cases it is crucial that the quantity and quality of the said metals is cautiously analysed/controlled and reported (along with the appropriate control experimentation).

Last, the effect of carbonaceous debris (in addition to edge plane defects as covered at the end of Sect. 3.2.1) has been explored upon the electrochemical behaviour of reduced graphene oxide (GO), and was reported to strongly affect the observed electrochemical response [64]. It is important to take from this work that when GO is reduced to graphene, pristine graphene does not result, rather a graphene that possesses strongly adhered carbonaceous debris and edge plane defect sites which are created during the synthesis of GO [64]. Other comparable work has also shown this to be the case, where the carbonaceous debris significantly impacted the observed electrochemical response (beneficial in this case for electroanalysis, as is expected given the insights gained in Sect. 3.2.1) [64]. Interesting work has been performed by Tan and co-workers [65] utilising SECM to study the reactivity of surface imperfections present (i.e. edge plane defects or carbonaceous debris) on monolayer graphene, revealing that specific sites across the surface of monolayer graphene that have a large concentration of defects (introduced either through deliberate mechanical damage or through chemical oxidation (as with reduced GO)) are approximately 1 order of magnitude more reactive, compared to more pristine graphene surfaces, toward electrochemical reactions [65]. Of further importance, the authors were able to successfully passivate the activity of graphene defects by carefully controlling the electro-polymerisation of o-phenylenediamine so that a thin film of the polymer was formed (which was found to be insulating in nature toward heterogeneous electron transfer processes): thus it was demonstrated that SECM can be utilised for detecting the presence of (and "healing") surface defects on graphene; providing a strategy for in situ characterisation and control of this fascinating material and enabling optimisation of its properties for select applications as stated in Sect. 3.2.1 [65].

3.2.4 Electrochemical Reports of Modified (N-doped) Graphene

As mentioned earlier, through the modification of graphene one can tailor its properties to produce *task specific graphene*. Although there are a wide range of modified graphenes that can be synthesised (the electrochemical applications of which are fully explored in Chap. 4), in this section we focus solely on the use of nitrogen doped (*N*-doped) graphene to give readers a general overview of how the resultant properties of the modified graphene differ from that of pristine graphene and hence can lead to beneficial outcomes.

The chemical doping of graphene falls into two key areas: (i) the adsorption of organic, metallic and gaseous molecules/compounds onto the graphene surface; and (ii) substitutional doping, where heteroatoms are introduced into the graphene lattice, such as nitrogen and boron [66–69]. Both approaches have been reported to alter the electronic properties of graphene (including the DOS, which in turn influences the heterogeneous electron transfer properties observed as was highlighted in Chap. 2) [66, 70], where for example doping with boron or nitrogen atoms allows graphene transformation into either a *p*- or *n*-type semiconductor respectively [70–73]. Generally the doping of graphene with nitrogen is favoured and widely pursued because it is (a nitrogen atom) of comparable atomic size and the fact that it contains five valence electrons that are available to form strong valence bonds with carbon atoms [74].

Wang and co-workers provide a thorough overview of the synthesis of *N*-doped graphene [66], in which the authors overview the many fabrication routes available, which include direct synthesis (such as through CVD), solvothermal approaches, arc-discharge, and post-synthesis treatments such as thermal, plasma and chemical methods [66, 75]; Table 3.1 overviews these various methodologies.

Through the doping of graphene to produce *N*-doped graphene, three common bonding configurations arise, which are: quaternary *N* (or graphitic *N*), pyridinic *N*, and pyrrolic *N*. As shown in Figs. 3.25 and 3.26, pyridinic *N* bonds with two C atoms at the edges or defects of graphene contribute one *p* electron to the π system while Pyrrolic *N* refers to *N* atoms that contribute two p electrons to the π system, although unnecessarily bond into the five-membered ring, as in pyrrole. Quaternary *N* refers to *N* atoms that substitute for C atoms in the hexagonal ring. Among these nitrogen types, pyridinic *N* and quaternary *N* are sp^2 hybridised and pyrrolic *N* is sp^3 hybridised. Apart from these three common nitrogen types, *N* oxides of pyridinic *N* have been observed in both the *N*-graphene and N-CNT studies where the nitrogen atom bonds with two carbon atoms and one oxygen atom [66, 96, 97].

In terms of the electrochemical application of doped graphene, one area where *N*-doped graphene is being extensively studied is as a replacement for platinum in fuel cells [68, 77, 91, 98–101]. Other work has reported the electrochemical oxidation of methanol (again for fuel cell applications), fast electron transfer kinetics for glucose oxidase, and high sensitivity and selectivity for glucose bio-sensing, in addition to the direct sensing of hydrogen peroxide [68, 77, 91, 98–101].

3.2.5 The Electrochemical Response of Graphene Oxide

GO is by no means a new material, with first reports emerging around 1859. Structurally it constitutes single atomic layers of functionalised (oxygenated) graphene that can readily extend up to tens of μm in lateral dimension. GO can be viewed as an unconventional type of soft material as it carries the characteristics of polymers, colloids, membranes and is an amphiphile [102, 103]. The specific structure of GO is debatable and Fig. 1.4 (found in Chap. 1) shows the various

Table 3.1 Nitrogen-doping methods and nitrogen (N) concentration on graphene. Reprinted with permission from Ref. [66]. Copyright 2012 American Chemical Society

No.	Synthesis method	Precursors	N content, at. %	Application/reference
1	CVD	Cu film on Si substrate as catalyst, CH_4/NH_3	1.2–8.9	FET / [70]
2	CVD	Cu foil as catalyst, NH_3/He	1.6–16	ORR / [76]
3	CVD	Ni film on SiO_2/Si substrate as catalyst, $NH_3/CH_4/H_2$/Ar (10:50:65:200)	4	ORR / [77]
4	CVD	Cu foil as catalyst, acetonitrile	~9	Lithium battery / [78]
5	CVD	Cu foil as catalyst, pyridine	~2.4	FET / [79]
6	Segregation growth	Carbon-contained Ni layer on nitrogen-contained boron layer	0.3–2.9	FET / [80]
7	Solvothermal	Li_3N/CCl_4 (NG1) or $N_3C_3Cl_3/Li_3N/CCl_4$ (NG2)	4.5 (NG1) or 16.4 (NG2)	ORR / [81]
8	Arc discharge	Graphite/H_2He/pyridine (NG1) graphite/H_2/He/NH_3 (NG2) transformation of nanodiamond/He/pyridine (NG3)	0.6 (NG1), 1 (NG2), 1.4 (NG3)	[82, 83]
9	Thermal treatment	N^+ ion-irradiated graphene, NH_3	1.1	FET / [84]
10	Thermal treatment	Graphite oxide after thermal expansion, NH_3/Ar	2.0–2.8	ORR / [85]
11	Thermal treatment	GNR, NH_3	NSD	FET / [86]
12	Thermal treatment	GO, NH_3/Ar (10 % NH_3)	~3–5	FET / [87]
13	Thermal treatment	GO, NH_3	6.7–10.78	Methanol oxidation / [88]
14	Thermal treatment	GO, melamine	7.1–10.1	ORR / [89]
15	Plasma treatment	Graphite oxide after thermal expansion, N_2 plasma	8.5	ORR / [68]
16	Plasma treatment	Graphite oxide after thermal expansion, N_2 plasma	3	ORR / [90]
17	Plasma treatment	Chemically synthesised graphene, N_2 plasma	~1.3	Biosensors / [91]
18	Plasma treatment	GO, treat with H_2 plasma first, then treat with N_2 plasma	1.68–2.51	Ultracapacitor / [92]
19	Plasma treatment	Mechanically exfoliated graphene or bilayer graphene grown by CVD, NH_3 plasma	NSD	FET / [93]
20	N_2H_4 treatment	GO, N_2H_4, NH_3	4.01–5.21	[94]
21	N_2H_4 treatment	Graphite oxide after thermal expansion, N_2H_4	1.04	Electrochemical sensor / [95]

Abbreviations: *CVD* chemical vapour deposition; *GNR* graphene nanoribbons; *GO* graphene oxide; *NSD* not stated; *FET* field-effect transistor; *ORR* oxygen reduction reaction

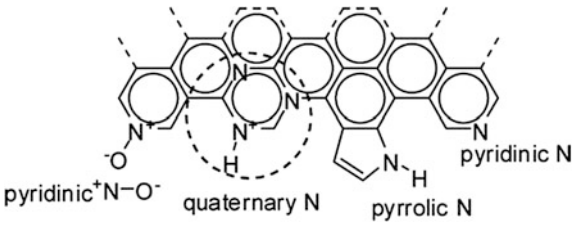

Fig. 3.25 Bonding configurations for nitrogen atoms in *N*-graphene. Reprinted with permission from Ref. [66]. Copyright 2012 American Chemical Society

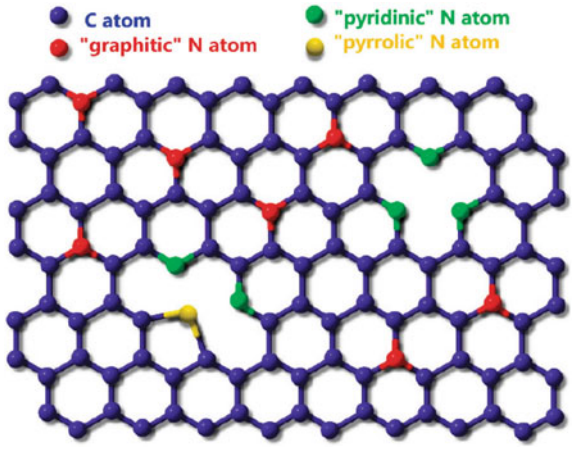

Fig. 3.26 Schematic representation of *N*-doped graphene. The *blue*, *red*, *green*, and *yellow spheres* represent the C, "graphitic" N, "pyridinic" N, and "pyrrolic" N atoms in the *N*-doped graphene, respectively. Evidence of the N-doped graphene structure is supported by XPS. Reprinted with permission from Ref. [70]. Copyright 2009 American Chemical Society

models that can exist along with the most recent proposition shown in Fig. 3.27 which accounts for weaknesses in the models proposed in Fig. 1.4 [104].

As highlighted in Chap. 1 GO is useful, in that, a common approach to fabricate graphene is to chemically, thermally or electrochemically reduce GO. Of note is work by Zhou et al. [105] who have reported the electrochemical reduction of GO films, which has resulted in a material that has a low O/C ratio. Such reduction proceeds via the following electrochemical process (where ER implies electrochemically reduced):

$$\mathrm{GO} + a\mathrm{H}^{+} + be^{-} \rightarrow \mathrm{ER{:}GO} + c\mathrm{H_2O} \tag{3.7}$$

Of importance here is that the electrochemical reduction gives rise to voltammetric reduction waves at highly negative potentials. Figure 3.28 depicts the electrochemical reduction of GO where the cathodic peak potentials are observed to shift negatively as the pH increases [105]. This is believed to be a consequence of the protonation involved in the electro-reduction process (see Eq. 3.7), which is facilitated at lower pH values.

Exploring the electrochemistry of GO further, it is important to note that in other work the cyclic voltammetric response of GO has been shown to be unique towards specific electron transfer redox probes [106]. Given this fact, such unique

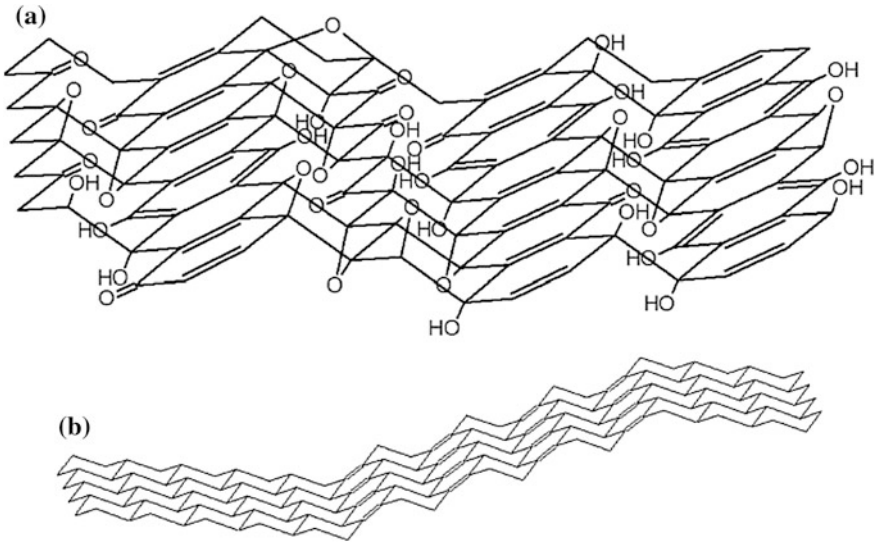

Fig. 3.27 A new structural model of GO: **a** surface species and **b** folded carbon skeleton. Reprinted with permission from Ref. [104]. Copyright 2006 American Chemical Society

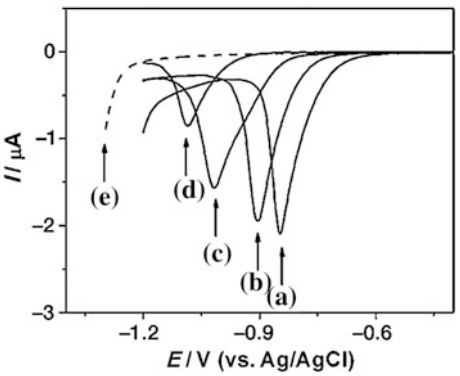

Fig. 3.28 Linear sweep voltammograms (in phosphate buffer solution (PBS)) of a GC electrode in contact with ~7-mm-thick GO film supported on quartz (5×4 cm^2) at pH values of 4.12 (*a*), 7.22 (*b*), 10.26 (*c*) and 12.11 (*d*). Note that (*e*) represents a response recorded at the unmodified/bare GC electrode suspended in Na-PBS (1 M, pH 4.12). Reproduced from Ref. [105] with permission from Wiley

voltammetry can thus be used (as a characterisation technique) to ensure that GO has been fully transformed to graphene by exploring the voltammetric response before and after the chosen treatment has been applied [106]. Figure 3.29a shows the voltammetric response of increasing amounts of GO immobilised on an electrode surface (using the outer-sphere redox probe hexaammine-ruthenium(III) chloride), which is directly compared with that of increasing graphene additions

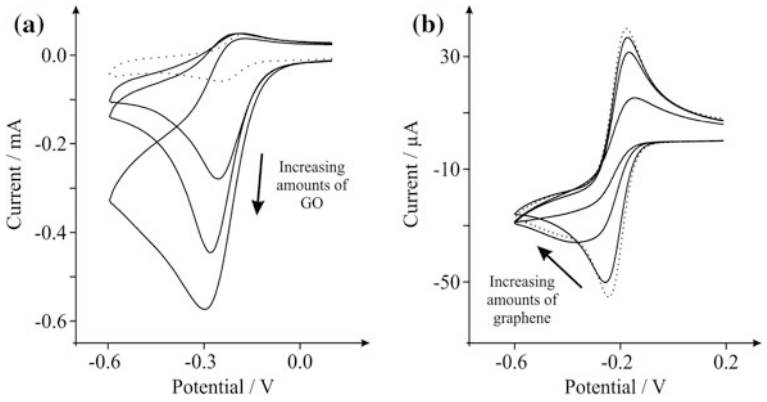

Fig. 3.29 Cyclic voltammetric profiles recorded towards 1 mM hexaammine-ruthenium(III) chloride in 1 M KCl. Scan rate: 100 mVs^{-1} (*vs.* SCE). **a** obtained using an EPPG electrode (*dotted line*) after modification with increasing depositions of 1.38, 2.75 and 8.25 µg GO (*solid lines*). Reproduced from Ref. [106] with permission from The Royal Society of Chemistry. **b** Obtained using an EPPG electrode (*dotted line*) with the addition of increasing amounts of 100, 200 and 300 ng graphene (*solid lines*). Reproduced from Ref. [33] with permission from The Royal Society of Chemistry

(Fig. 3.29b). It can be readily observed that unique voltammetry is evident at the GO modified electrode, which is quite different to that observed at the graphene modified electrode, where it is thought that in the case of GO the oxygenated species present contribute to a catalytic process, the EC' reaction (see Sect. 2.5), where a first 'electron transfer process' (E process), as described generally as [106]:

$$A + e^- \rightleftharpoons B \quad (E\,Step) \tag{3.8}$$

is then followed by a 'chemical process' (C process) involving the electro-generated product, B, which regenerates the starting reactant, A, as described by [106]:

$$B + C \xrightarrow{k} A + products \quad (C\,Step) \tag{3.9}$$

The voltammetric response arises as the amount of C is increased; which is attributed to the oxygenated species of the GO in this case [106]. Bear in mind that this response is unique to hexaammine-ruthenium(III) chloride and also occurs to a lesser extent for potassium hexachloroiridate(III) [106]. Crucially, the observed voltammetric reduction waves evident in Fig. 3.28 coupled with the voltammetry observed in Fig. 3.29 can be used as a measure to determine whether GO has been efficiently (electrochemically) reduced prior to its application in a plethora of areas [105, 106].

3.2.6 Electrochemical Characterisation of CVD Grown Graphene

The electrochemistry of CVD fabricated graphene can yield beneficial insights into the surface structure of the grown graphene layer [107, 108]. It has been demonstrated that through the careful choice of redox probes, different voltammetric responses can be observed, allowing insights into the structure and composition of the surface under investigation to be readily derived [107, 108].

In the case of CVD grown graphene that possesses a uniform (and complete) coverage of graphene, however with graphitic islands present randomly distributed across the surface; when using the outer-sphere redox probe 'hexaammine-ruthenium(III) chloride' to characterise the surface of the graphene electrode, a typical peak shaped cyclic voltammetric profile is observed and would indicate that a uniform 'graphene' film has been successfully fabricated (Fig. 3.30a). In this case, the outer-sphere electron transfer probe is surface insensitive (see Box 3.1) and thus the graphene electrode (namely *all* of the edge plane sites present) merely acts as a source (or sink) of electrons such that the majority of the geometric electrode area participates in the electrochemical reaction; resulting in heavily overlapping diffusional zones (see Fig. 3.30c, which is of course dependent on the applied scan rate) and hence a macro-electrode type response (cyclic peak shaped) is observed [107]. It is only by using redox probes with varying surface sensitivities however that material scientists are able to fully characterise their CVD grown graphene; we now consider the electrochemical response when utilising an inner-sphere redox probe.

If the redox probe is changed to an inner-sphere probe such as 'potassium ferrocyanide(II)', it is possible that a completely different voltammetric response is observed, as shown in Fig. 3.30b, where a steady-state voltammetric response is evident; this is usually seen at microelectrodes (see Chap. 2)—note that the voltammetric response in Fig. 3.30b is obtained after potential cycling. It is well documented that potassium ferrocyanide is highly surface sensitive (see Box 3.1) and exhibits a response dependent on the Carbon-Oxygen surface groups present on the surface of an electrode, ranging from beneficial to detrimental responses [41]. Since only a certain number of graphitic domains (that is, double-, few- and multi-layered graphene) residing on the surface are activated with the correct proportion of Carbon-Oxygen groups through potential cycling, only certain areas of the electrode surface become activated. This effectively produces a random array of active areas across the electrode surface, which have their own diffusion zones (see Fig. 3.30c), the majority of which are separated far from each other (under the applied voltammetric scan rate utilised in the given work) [107] such that these diffusion zones do not interact and thus sigmoidal voltammetry is observed. In this case, assuming that each activated zone/domain is akin to a microelectrode array, the electrochemical response, that is, a limiting current (see Chap. 2) is given by:

$$I_L = nFrCDN \tag{3.10}$$

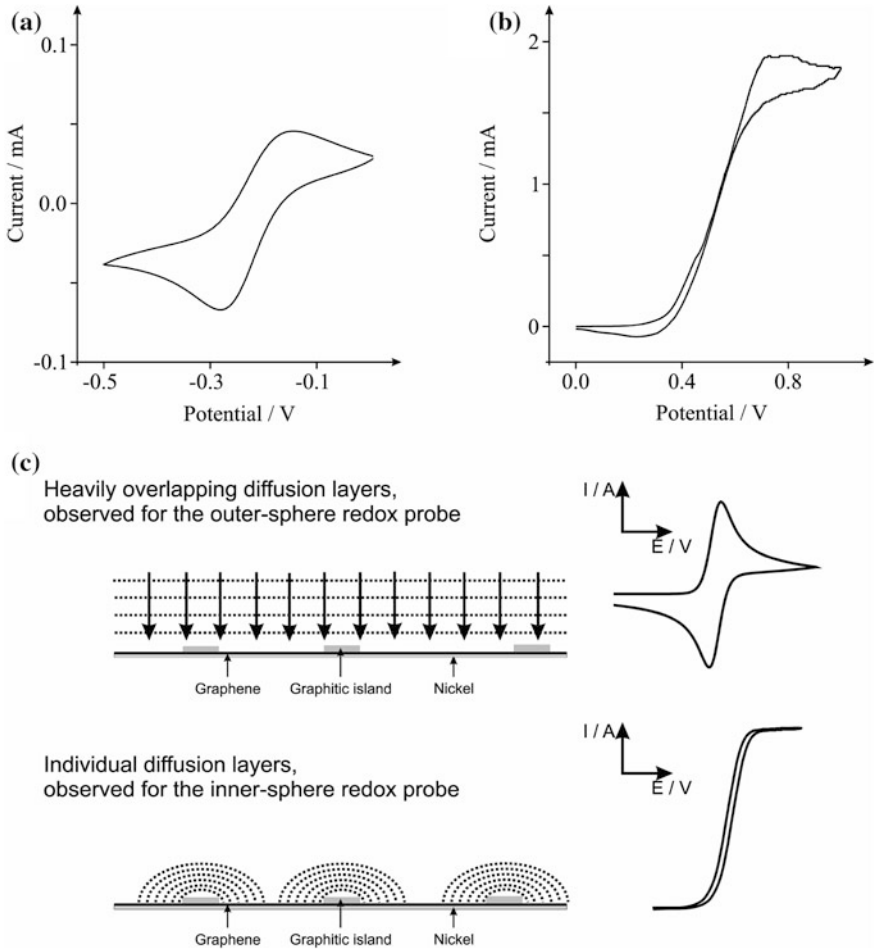

Fig. 3.30 **a** Cyclic voltammetric profiles recorded utilising 1 mM hexaammine-ruthenium(III) chloride in 1 M KCl, obtained using a CVD-graphene electrode (*dashed line*). **b** Cyclic voltammetric profiles recorded for 1 mM potassium ferrocyanide(II) in 1 M KCl using a CVD-graphene electrode. **c** A schematic representation of differing diffusion zones observable towards graphitic islands present upon CVD-graphene. **a** and **b** performed at a scan rate of 100 mVs^{-1} (*vs.* SCE). Figure reproduced from Ref. [107] with permission from The Royal Society of Chemistry

where n is the number of electrons, F the Faraday constant, C is the concentration of the analyte, D the diffusion coefficient of the analyte and r is the electrode radii. Note that N is the number of electrodes/activated zones/domains comprising the CVD surface and the magnitude of the voltammetry observed in Fig. 3.30b is simply "amplified" by N if the criteria that each diffusion zone is independent of each other and not overlapping, is apparent. It is apparent that the current is larger at the steady-state response (Fig. 3.30b) over that of the peak shaped response

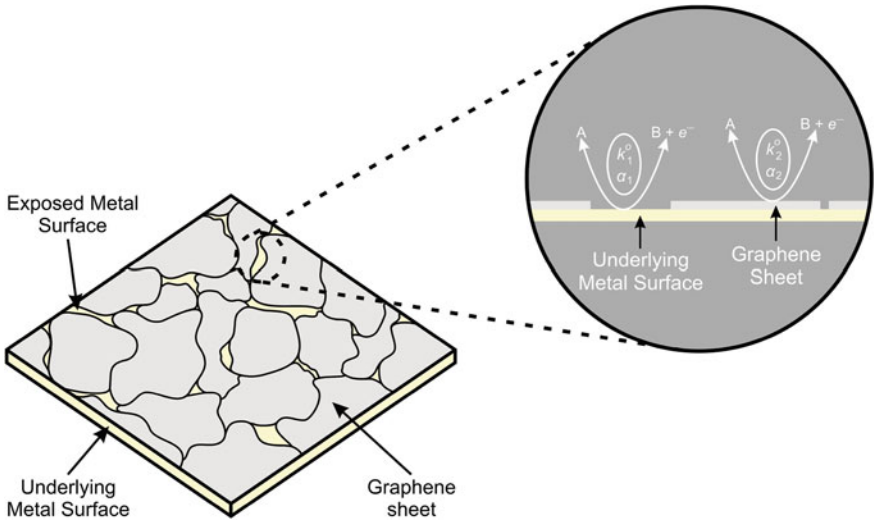

Fig. 3.31 A schematic representation of non-continuous CVD grown graphene electrode where the underlying metal surface is exposed to the solution, both with different Butler-Volmer characteristics. Note that the depending on the shape, size and reactivity of the given exposed surface (and that of the graphene), different voltammetry will be observed as per Chap. 2

(Fig. 3.30a) which is due to the above description, through being an array of microelectrdes/activated domains.

The importance of utilising different electrochemical redox probes in order to gain insights and effectively characterise potential electrode materials (viz Box 3.1) has thus been shown above. For instance if indeed a complete coverage of uniform single-layered pristine graphene had been present in the above case no voltammetric responses would have been observed. If defects occur across the basal plane surface then the voltammetry would appear very slow, slower than that observed for a BPPG with the response becoming more reversible (towards that of EPPG) as the global coverage of edge plane like- defects increased. Furthermore, other scenarios could exist, as explored below.

An interesting scenario can occur when material scientists grown their graphene via CVD and fail to perform adequate control experiments, as is common in the literature. That is, a beneficial electrochemical response is observed using the CVD grown graphene and control experiments using the underlying metal surface that the graphene has been grown upon, typically nickel [109, 110] or copper [11, 111] have been neglected to be performed using the same redox probe used to characterise the graphene surface. Figure 3.31 shows the case of a non-continuous graphene film where the underlying metal surface upon which the graphene was grown is exposed to the solution [107, 108]. In this case, we have a heterogeneous electrode surface which is reminiscent of the case of the HOPG surface as discussed in Sect. 3.1.2 where again, the two surfaces will have their own electrochemical activity (heterogeneous rate constant) towards the given redox probes;

that is, the graphene film, $k^0_{graphene}$ and the underlying metal surface $k^0_{metal\,surface}$ upon which the graphene has been grown.

In the first case, if the graphene film has a greater electrochemical activity over that of the underling metal surface, such that $k^0_{graphene} \gg k^0_{metal\,surface}$, the grown graphene domains will dominate the electrochemical response. Assuming that the coverage of graphene is of the macro-electrode scale this will giving rise to peak shaped voltammetry as the surface will be akin to a macroelectrode. However, note that as the graphene sheet becomes non-continuous and graphene islands are formed (which are randomly distributed across the underlying metal surface), each graphene domain will have its own diffusion zone and if these are not heavily overlapping (see Fig. 3.30c) such that these diffusion zones do not interact, sigmoidal voltammetry will dominate. Thus the above case will likely be observed as discussed in Fig. 3.30 with select redox probes: depending on the graphene's size, shape and orientation (as well as surface coverage) different voltammetry will be observed, as covered in Chap. 2. Note of course that this will also depend upon the chosen voltammetric scan rate, the diffusion coefficient of the electroactive target/analyte and the coverage of the dominant electrochemically active material.

In the second case of a non-continuous graphene film, the underlying metal surface (due to its reactivity) will act like an electrode and if the metal has favourable electrochemical properties towards the electrochemical analyte which is of interest, it will contribute to the observed electrochemical response or even dominate it; misleading researchers into thinking that graphene exhibits excellent electrochemical properties [107, 108]. In this case, assuming $k^0_{graphene} \ll k^0_{metal\,surface}$ the metal surface will dictate the electrochemical response depending on the coverage of the graphene film/islands. If the coverage of graphene is large, such that only nano- or micro- bands of the underlying metal are exposed, a microelectrode type response will be observed in the form of a steady-state response (sigmoidal voltammetry) where the magnitude of the current is amplified by the number of exposed domains and will be governed by Eq. (3.10). However, this will depend upon the distribution of the graphene islands and an alternative case might result in even macro-electrode type structures/areas of the underlying metal being exposed! This last case will obviously result in peak shaped voltammetry dominating, which after being originally theorised in Ref. [107], has been shown recently at ill formed graphene grown upon nickel and copper such that the exposed underlying electrode dominates over that of graphene (in this case due to the poor fabrication, the exposed surfaces are large irregular macro-sized domains) [112]. The key to determining if the underlying surface is contributing towards the observed electrochemical response is to run control experiments, that is, perform the same voltammetry using the underlying supporting material (viz no graphene) to determine the extent of the electrochemical activity.

Last, a really unique response might be observed, which was discussed in Sect. 3.1.2 with respect to HOPG electrode surfaces, such that two voltammetric peaks might be observed! In this case a first peak would arise from a material exhibiting fast electron transfer and a second peak from the graphene surface. The

extent of the observed voltammetry will depend on the electrochemical activity of the two materials comprising the heterogeneous surface, the distance between active sites (diffusion zones), voltammetric scan rates, the diffusion coefficient of the electroactive target/analyte and the coverage of the dominant electrochemically active material.

It is evident, due to the above scenarios, that the electrochemistry of CVD grown graphene is highly fascinating. This section has also highlighted that materials scientists can beneficially utilise electrochemistry as a tool to assist in the characterisation of their fabricated 'graphene' material.

References

1. R.L. McCreery, Chem. Rev. **108**, 2646–2687 (2008)
2. D.A.C. Brownson, C.E. Banks, Analyst **135**, 2768–2778 (2010)
3. Web-Resource, http://www.nanoprobes.aist-nt.com/apps/HOPG%2020info.htm. Accessed 18 Jan 2013
4. T.J. Davies, M.E. Hyde, R.G. Compton, Angew. Chem. Int. Ed. **44**, 5121–5126 (2005)
5. T.J. Davies, R.R. Moore, C.E. Banks, R.G. Compton, J. Electroanal. Chem. **574**, 123–152 (2004)
6. C.E. Banks, R.G. Compton, Analyst **131**, 15–21 (2006)
7. Web-Resource, www.graphene-supermarket.com. Accessed 28 Feb 2012
8. A. Dato, V. Radmilovic, Z. Lee, J. Phillips, M. Frenklach, Nano Lett. **8**, 2012–2016 (2008)
9. M. Lotya, P.J. King, U. Khan, S. De, J.N. Coleman, ACS Nano **4**, 3155–3162 (2010)
10. Web-Resource, www.nanointegris.com. Accessed 28 Feb 2012
11. X. Li, C.W. Magnuson, A. Venugopal, R.M. Tromp, J.B. Hannon, E.M. Vogel, L. Colombo, R.S. Ruoff, J. Am. Chem. Soc. **133**, 2816–2819 (2011)
12. D.A.C. Brownson, C.E. Banks, Phys. Chem. Chem. Phys. **14**, 8264–8281 (2012)
13. D.A.C. Brownson, D.K. Kampouris, C.E. Banks, Chem. Soc. Rev. **41**, 6944–6976 (2012)
14. K.K. Cline, M.T. McDermott, R.L. McCreery, J. Phys. Chem. **98**, 5314–5319 (1994)
15. M.C. Henstridge, E. Laborda, N.V. Rees, R.G. Compton, Electrochimica. Acta **84**, 12–20 (2012)
16. R. Nissim, C. Batchelor-McAuley, M.C. Henstridge, R.G. Compton, Chem. Commun. **48**, 3294–3296 (2012)
17. R.L. McCreery, M.T. McDermott, Anal. Chem. **84**, 2602–2605 (2012)
18. N.M.R. Peres, L. Yang, S.-W. Tsai, New J. Phys. **11**, 095007 (2009)
19. D. Jiang, B.G. Sumpter, S. Dai, J. Chem. Phys. **126**, 134701 (2007)
20. M. Pumera, Chem. Soc. Rev. **39**, 4146–4157 (2010)
21. Y. Shimomura, Y. Takane, K. Wakabayashi, J. Phys. Soc. Jpn. **80**, 054710 (2011)
22. R. Sharma, J.H. Baik, C.J. Perera, M.S. Strano, Nano Lett. **10**, 398–405 (2010)
23. C.E. Banks, T.J. Davies, G.G. Wildgoose, R.G. Compton, Chem. Commun., 2005, 829–841
24. K.R. Ward, N.S. Lawrence, R.S. Hartshorne, R.G. Compton, Phys. Chem. Chem. Phys. **14**, 7264–7275 (2012)
25. M.A. Edwards, P. Bertoncello, P.R. Unwin, J. Phys. Chem. C **113**, 9218–9223 (2009)
26. C.G. Williams, M.A. Edwards, A.L. Colley, J.V. Macpherson, P.R. Unwin, Anal. Chem. **81**, 2486–2495 (2009)
27. S.C.S. Lai, A.N. Patel, K. McKelvey, P.R. Unwin, Angew. Chem. Int. Ed. **51**, 5405–5408 (2012)
28. C. Batchelor-McAuley, E. Laborda, M.C. Henstridge, R. Nissim, R.G. Compton, Electrochim. Acta **88**, 895–898 (2013)

29. W. Li, C. Tan, M.A. Lowe, H.D. Abruna, D.C. Ralph, ACS Nano **5**, 2264–2270 (2011)
30. A.T. Valota, I.A. Kinloch, K.S. Novoselov, C. Casiraghi, A. Eckmann, E.W. Hill, R.A.W. Dryfe, ACS Nano **5**, 8809–8815 (2011)
31. F. Banhart, J. Kotakoski, A.V. Krasheninnikov, ACS Nano **5**, 26–41 (2011)
32. R.S. Robinson, K. Sternitzke, M.T. McDermott, R.L. McCreery, J. Electrochem. Soc. **138**, 2412–2418 (1991)
33. D.A.C. Brownson, L.J. Munro, D.K. Kampouris, C.E. Banks, RSC Adv. **1**, 978–988 (2011)
34. J.C. Meyer, C. Kisielowski, R. Erni, M.D. Rossell, M.F. Crommie, A. Zettl, Nano Lett. **8**, 3582–3586 (2008)
35. M.M. Ugeda, I. Brihuega, F. Guinea, J.M. Gomez-Rodriguez, Phys. Rev. Lett. **104**, 096804 (2010)
36. D.A.C. Brownson, L.C.S. Figueiredo-Filho, X. Ji, M. Gomez-Mingot, J. Iniesta, O. Fatibello-Filho, D.K. Kampouris, C.E. Banks, J. Mater. Chem. A **1**, 5962–5972 (2013)
37. D.K. Kampouris, C.E. Banks, Chem. Commun. **46**, 8986–8988 (2010)
38. P.M. Hallam, C.E. Banks, Electrochem. Commun. **13**, 8–11 (2011)
39. A.G. Guell, N. Ebejer, M.E. Snowden, J.V. Macpherson, P.R. Unwin, J. Am. Chem. Soc. **134**, 7258–7261 (2012)
40. C.X. Lim, H.Y. Hoh, P.K. Ang, K.P. Loh, Anal. Chem. **82**, 7387–7393 (2010)
41. X. Ji, C.E. Banks, A. Crossley, R.G. Compton, Chem. Phys. Chem. **7**, 1337–1344 (2006)
42. A. Chou, T. Böcking, N.K. Singh, J.J. Gooding, Chem. Commun., 2005, 842–844
43. L. Tang, Y. Wang, Y. Li, H. Feng, J. Lu, J. Li, Adv. Funct. Mater. **19**, 2782–2789 (2009)
44. S.P. Kumar, R. Manjunatha, C. Nethravathi, G.S. Suresh, M. Rajamathi, T.V. Venkatesha, Electroanalysis **23**, 842–849 (2011)
45. J. Premkumar, S.B. Khoo, J. Electroanal. Chem. **576**, 105–112 (2005)
46. P. Chen, R.L. McCreery, Anal. Chem. **68**, 3958–3965 (1996)
47. P. Chen, M.A. Fryling, R.L. McCreery, Anal. Chem. **67**, 3115–3122 (1995)
48. G.P. Keeley, A. O'Neill, N. McEvoy, N. Peltekis, J.N. Coleman, G.S. Duesberg, J. Mater. Chem. **20**, 7864–7869 (2010)
49. G.P. Keeley, A. O'Neill, M. Holzinger, S. Cosnier, J.N. Coleman, G.S. Duesberg, Phys. Chem. Chem. Phys. **13**, 7747–7750 (2011)
50. A. Ambrosi, A. Bonanni, M. Pumera, Nanoscale **3**, 2256–2260 (2011)
51. H.L. Poh, F. Sanek, A. Ambrosi, G. Zhao, Z. Sofer, M. Pumera, Nanoscale **4**, 3515–3522 (2012)
52. B. Guo, L. Fang, B. Zhang, J.R. Gong, Insciences J. **1**, 80–89 (2011)
53. X. Huang, X. Qi, F. Boey, H. Zhang, Chem. Soc. Rev. **41**, 666–686 (2012)
54. D.A.C. Brownson, J.P. Metters, D.K. Kampouris, C.E. Banks, Electroanalysis **23**, 894–899 (2011)
55. D.A.C. Brownson, C.E. Banks, Electrochem. Commun. **13**, 111–113 (2011)
56. D.A.C. Brownson, C.E. Banks, Analyst **136**, 2084–2089 (2011)
57. D.A.C. Brownson, C.E. Banks, Chem. Commun. **48**, 1425–1427 (2012)
58. C.H.A. Wong, M. Pumera, Electrochem. Commun. **22**, 105–108 (2012)
59. B. Sljukic, C.E. Banks, R.G. Compton, Nano Lett. **6**, 1556–1558 (2006)
60. C.E. Banks, A. Crossley, C. Salter, S.J. Wilkins, R.G. Compton, Angew. Chem. Int. Ed. **45**, 2533–2537 (2006)
61. A. Ambrosi, S.Y. Chee, B. Khezri, R.D. Webster, Z. Sofer, M. Pumera, Angew. Chem. Int. Ed. **51**, 500–503 (2012)
62. A. Ambrosi, C.K. Chua, B. Khezri, Z. Sofer, R.D. Webster, M. Pumera, Proc. Natl. Acad. Sci. USA **109**, 12899–12904 (2012)
63. M. Giovanni, H.L. Poh, A. Ambrosi, G. Zhao, Z. Sofer, F. Sanek, B. Khezri, R.D. Webster, M. Pumera, Nanoscale **4**, 5002–5008 (2012)
64. X. Li, X. Yang, L. Jia, X. Ma, L. Zhu, Electrochem. Commun. **23**, 94–97 (2012)
65. C. Tan, J. Rodriguez-Lopez, J.J. Parks, N.L. Ritzert, D.C. Ralph, H.D. Abruna, ACS Nano **6**, 3070–3079 (2012)
66. H. Wang, T. Maiyalagan, X. Wang, ACS Catal. **2**, 781–794 (2012)

67. L. Gan, D. Zhang, X. Guo, Small **8**, 1326–1330 (2012)
68. Y. Shao, S. Zhang, M.H. Engelhard, G. Li, G. Shao, Y. Wang, J. Liu, I.A. Aksay, Y. Lin, J. Mater. Chem. **20**, 7491–7496 (2010)
69. H. Liu, Y. Liu, D. Zhu, J. Mater. Chem. **21**, 3335–3345 (2011)
70. D. Wei, Y. Liu, Y. Wang, H. Zhang, L. Huang, G. Yu, Nano Lett. **9**, 1752–1758 (2009)
71. S. Mukherjee, T.P. Kaloni, J. Nanopart. Res. **2012**, 14 (1059)
72. L. Zhao, Science **333**, 999–1003 (2011)
73. A. Lherbier, X. Blase, Y.-M. Niquet, F. Triozon, S. Roche, Phys. Rev. Lett. **101**, 036808 (2008)
74. S.U. Lee, R.V. Belosludov, H. Mizuseki, Y. Kawazoe, Small **5**, 1769–1775 (2009)
75. C. Wang, Y. Zhou, L. He, T.-W. Ng, G. Hong, Q.-H. Wu, F. Gao, C.-S. Lee, W. Zhang, Nanoscale **5**, 600–605 (2013)
76. Z. Luo, S. Lim, Z. Tian, J. Shang, L. Lai, B. MacDonald, C. Fu, Z. Shen, T. Yu, J. Lin, J. Mater. Chem. **21**, 8038–8044 (2011)
77. L. Qu, Y. Liu, J.-B. Baek, L. Dai, ACS Nano **4**, 1321–1326 (2010)
78. A.L.M. Reddy, A. Srivastava, S.R. Gowda, H. Gullapalli, M. Dubey, P.M. Ajayan, ACS Nano **4**, 6337–6342 (2010)
79. Z. Jin, J. Yao, C. Kittrell, J.M. Tour, ACS Nano **5**, 4112–4117 (2011)
80. C. Zhang, L. Fu, N. Liu, M. Liu, Y. Wang, Z. Liu, Adv. Mater. **23**, 1020–1024 (2011)
81. D. Deng, X. Pan, L. Yu, Y. Cui, Y. Jiang, J. Qi, W.-X. Li, Q. Fu, X. Ma, Q. Xue, G. Sun, X. Bao, Chem. Mater. **23**, 1188–1193 (2011)
82. L.S. Panchakarla, K.S. Subrahmanyam, S.K. Saha, A. Govindaraj, H.R. Krishnamurthy, U.V. Waghmare, C.N.R. Rao, Adv. Mater. **21**, 4726–4730 (2009)
83. A. Ghosh, D.J. Late, L.S. Panchakarla, A. Govindaraj, C.N.R. Rao, J. Exp. Nanosci. **4**, 313–322 (2009)
84. B. Guo, Q. Liu, E. Chen, H. Zhu, L. Fang, J.R. Gong, Nano Lett. **10**, 4975–4980 (2010)
85. D. Geng, Y. Chen, Y. Chen, Y. Li, R. Li, X. Sun, S. Ye, S. Knights, Energy Environ. Sci. **4**, 760–764 (2011)
86. X. Wang, X. Li, L. Zhang, Y. Yoon, P.K. Weber, H. Wang, J. Guo, H. Dai, Science **324**, 768–771 (2009)
87. X. Li, H. Wang, J.T. Robinson, H. Sanchez, G. Diankov, H.J. Dai, J. Am. Chem. Soc. **131**, 15939–15944 (2009)
88. L.S. Zhang, X.Q. Liang, W.G. Song, Z.Y. Wu, Phys. Chem. Chem. Phys. **12**, 12055–12059 (2010)
89. Z.H. Sheng, L. Shao, J.J. Chen, W.J. Bao, F.B. Wang, X.H. Xia, ACS Nano **5**, 4350–4358 (2011)
90. R.I. Jafri, N. Rajalakshmi, S. Ramaprabhu, J. Mater. Chem. **20**, 7114–7117 (2010)
91. Y. Wang, Y. Shao, D.W. Matson, J. Li, Y. Lin, ACS Nano **4**, 1790–1798 (2010)
92. H.M. Jeong, J.W. Lee, W.H. Shin, Y.J. Choi, H.J. Shin, J.K. Kang, J.W. Choi, Nano Lett. **11**, 2472–2477 (2011)
93. Y.C. Lin, C.Y. Lin, P.W. Chiu, Appl. Phys. Lett. **96**, 133110 (2010)
94. D. Long, W. Li, L. Ling, J. Miyawaki, I. Mochida, S.H. Yoon, Langmuir **26**, 16096–16102 (2010)
95. D.W. Wang, I.R. Gentle, G.Q. Lu, Electrochem. Commun. **12**, 1423–1427 (2010)
96. C.P. Ewels, M. Glerup, J. Nanosci. Nanotechnol. **5**, 1345–1363 (2005)
97. J. Casanovas, J.M. Ricart, J. Rubio, F. Illas, J.M. Jiménez-Mateos, J. Am. Chem. Soc. **118**, 8071–8076 (1996)
98. Z. Lin, M.-K. Song, Y. Ding, Y. Liu, M. Liu, C.-P. Wong, Phys. Chem. Chem. Phys. **14**, 3381–3387 (2012)
99. G.-X. Ma, J.-H. Zhao, J.-F. Zheng, Z.-P. Zhu, Carbon **51**, 435 (2013)
100. K. Parvez, S. Yang, Y. Hernandez, A. Winter, A. Turchanin, X. Feng, K. Mullen, ACS Nano **6**, 9541–9550 (2012)
101. B. Zheng, J. Wang, F.-B. Wang, X.-H. Xia, Electrochem. Commun. **28**, 24–26 (2013)
102. D.R. Dreyer, S. Park, C.W. Bielawski, R.S. Rouff, Chem. Soc. Rev. **39**, 228–240 (2010)

103. L.J. Cote, J. Kim, V.C. Tung, J. Luo, F. Kim, J. Huang, Pure Appl. Chem. **83**, 95–110 (2011)
104. T. Szabo, O. Berkesi, P. Forgo, K. Josepovits, Y. Sanakis, D. Petridis, I. Dekany, Chem. Mater. **18**, 2740–2749 (2006)
105. M. Zhou, Y. Wang, Y. Zhai, J. Zhai, W. Ren, F. Wang, S. Dong, Chem. Eur. J. **15**, 6116–6120 (2009)
106. D.A.C. Brownson, A.C. Lacombe, M. Gomez-Mingot, C.E. Banks, RSC Adv. **2**, 665–668 (2012)
107. D.A.C. Brownson, C.E. Banks, Phys. Chem. Chem. Phys. **13**, 15825–15828 (2011)
108. D.A.C. Brownson, M. Gomez-Mingot, C.E. Banks, Phys. Chem. Chem. Phys. **13**, 20284–20288 (2011)
109. A.N. Obraztsov, E.A. Obraztsova, A.V. Tyurnina, A.A. Zolotukhin, Carbon **45**, 2017–2021 (2007)
110. K.S. Kim, Y. Zhao, H. Jang, S.Y. Lee, J.M. Kim, K.S. Kim, J.-H. Ahn, P. Kim, J.-Y. Choi, B.H. Hong, Nature **457**, 706–710 (2009)
111. A. Guermoune, T. Chari, F. Popescu, S.S. Sabri, J. Guillemette, H.S. Skulason, T. Szkopek, M. Siaj, Carbon **49**, 4204–4210 (2011)
112. A. Ambrosi, A. Bonanni, Z. Sofer, M. Pumera, Nanoscale **5**, 2379–2387 (2013)